Theory, Observations, and Simulations of Kinetic Entropy in a Magnetotail Electron Diffusion Region

M. R. Argall,[1, a)] M. H. Barbhuiya,[2] P. A. Cassak,[2] S. Wang,[3] J. Shuster,[3] H. Liang,[4] D. J. Gershman,[3] R. B. Torbert,[1] and J. L. Burch[5]

[1)] *Space Science Center, Institute for the Study of Earth, Oceans, and Space, University of New Hampshire, Durham, NH 03824, USA*

[2)] *Department of Physics and Astronomy and Center for KINETIC Plasma Physics, West Virginia University, Morgantown, WV 26506, USA*

[3)] *Goddard Space Flight Center, NASA, Greenbelt, MD 20771, USA*

[4)] *Center for Space Plasma and Aeronomic Research, University of Alabama in Huntsville, Huntsville, AL 35899, USA*

[5)] *Space Science and Engineering Division, Southwest Research Institute, San Antonio, TX 78238, USA*

(Dated: 11 January 2022)

1

We examine velocity-space kinetic entropy, a spatially local measure of entropy for systems out of thermal equilibrium, during an encounter of an electron diffusion region (EDR) at a magnetic reconnection site in Earth's magnetotail by the Magnetospheric Multiscale (MMS) mission. We start by generalizing the theory of kinetic entropy to the case of non-uniform velocity space grids and transforming the equations into spherical energy coordinates useful to experimental plasma detectors. The theory is then applied to MMS data and compared to particle-in-cell simulations of reconnection. We demonstrate that the entropy based non-Maxwellianity measure from the MMS data is of sufficiently high precision to reliably identify non-Maxwellian distributions, and therefore the measurements when kinetic effects are most significant. By comparing two different non-Maxwellian measures, we show that total entropy density suffers from "information loss" because it lacks a dependence on the velocity space grid, and so has lost information about how well a distribution function is resolved. Local velocity-space kinetic entropy density recovers this information. We quantify information loss and argue that the considerations needed to minimize it are crucial for instruments designed to measure distribution functions in-situ.

a)Electronic mail: matthew.argall@unh.edu

I. INTRODUCTION

Energy at large scales gets dissipated at small scales in essentially all plasmas, and how this conversion and dissipation occurs often impacts the plasma dynamics at the large scales[1]. For example, the evolution of collisionless shocks[2], plasma turbulence[3], and magnetic reconnection[4] all influence – and are influenced by – small scale energy conversion and dissipation processes. Magnetic reconnection, where a change in magnetic field topology facilitates a rapid release of magnetic energy[5], plays a central role in the spoiling of confinement in tokamaks, the release of energy in solar flares, and the energy cycle within Earth's magnetosphere. In the magnetosphere, reconnection leads to the release of 10^{15} J of energy over just a few minutes[6] – enough to supply New York City for an entire year[7]. Even though energy conversion occurs at global scales, dissipation at electron scales contributes greatly[8]. Several scalar, reference-frame-invariant parameters were proposed as a means of locating reconnection sites[9–15] to identify and understand the dissipation processes. However, electron scales remained inaccessible to observations until the launch of the Magnetospheric Multiscale (MMS) mission[16], which now allows us to investigate kinetic processes that lead to dissipation and test aspects of kinetic theory, including kinetic entropy.

The importance of entropy is captured by the Second Law of Thermodynamics – in a closed, isolated system in which energy is conserved, entropy never decreases. From a thermodynamic perspective, high entropy is synonymous with a lack of energy that can be converted into mechanical work. From a kinetic theory perspective, entropy describes the disorder inherent to the system. The more ordered a system, the lower its entropy and the more effective the stored energy is able to perform mechanical work. As an example, in the electron diffusion region (EDR) of magnetic reconnection, electromagnetic fields do work on charged particles. This alters their particle distribution functions, often making them more ordered than Maxwellian distributions. non-Maxwellian distributions can be used to identify locations of electromagnetic energy dissipation[17–21] and may indicate that further dissipation of kinetic energy to thermal energy may occur. Entropy and non-Maxwellianity, therefore, should be able to identify locations like the EDR where key kinetic-scale energy conversion processes take place[22].

By comparing the current state of a system to its equilibrium, Maxwellianized state, non-Maxwellianity measures were developed. One contains the quadratic difference in distribu-

tion functions[14,15] while others contain the difference in entropies[23,24]. These were used to study dissipation in solar wind turbulence[14,15]; Earth's bow shock[25], dayside regions[26]; magnetotail plasma sheet[23]; collisional magnetic reconnection[27], and numerical simulations of collisionless magnetic reconnection[24]. It was shown that the form involving the difference in entropies, or the Kaufmann and Paterson non-Maxwellianity[23], can increase without bound the worse the velocity-space bins over- or under-resolve the distribution function[24]. An inadequate velocity-space bin size in simulations can lead to unphysical results for dissipation[22] even though the simulations are able to reproduce macroscopic properties of reconnection.

In perfectly collisionless systems, there is no dissipation —ideal kinetic physics is reversible. This was demonstrated in gyrokinetic simulations of magnetic reconnection in which the plasma has a reduced number of degrees of freedom[28]; however, reconnection becomes less reversible in fully kinetic simulations with decreasing guide field (increasing degrees of freedom)[29]. Irreversibility and non-conservation of entropy in simulations is tied to phase mixing[30] and numerical noise[31]. Numerical noise, however, is not present in real systems, yet observations of reconnection at the magnetopause revealed an unmeasured "residual" dissipation potentially linked to wave activity[32], which can lead to irreversible anomalous dissipation due to Landau damping[33].

Without collisions, the distribution function in kinetic plasmas can take on highly non-Maxwellian shapes. Elongated and striated distributions can be present near reconnection X-lines[10,34], while other shapes map to different regions and processes of reconnection[17,35–38], and are tied to energy dissipation[39,40] via scalar energy conversion parameters[11,41]. As mentioned, though, only entropy uniquely identifies irreversible dissipation. As the distributions become more structured, the number of arrangements that lead to the same distribution decreases, resulting in an increased non-Maxwellianity and decreased entropy[31]. non-Maxwellianity, structured distributions, and the processes that lead to dissipation, then, are all intricately related.

In this paper, we study the local velocity-space kinetic entropy in a magnetotail EDR during magnetic reconnection using electron-scale measurements from MMS. To do so, we derive a generalized kinetic entropy for arbitrary velocity-space grids, in particular the logarithmic spherical energy grid used by experimental plasma instruments. We show that kinetic entropy density and entropy-based non-Maxwellianity measures are in good agreement with a dedicated 2.5D particle-in-cell (PIC) simulation and that the non-Maxwellianity measure

is capable of identifying non-Maxwellian distributions in the MMS data. We further show that the entropy-based non-Maxwellianity calculated using kinetic entropy density is not positive definite as it should be, and that this is caused by the inappropriate velocity-space grid scale resolution. The velocity-space kinetic entropy captures the role of the velocity-space grid and gives physically meaningful results. We describe their difference in terms of a new concept, "information loss", which is used to quantify the extent to which the velocity-space grid over- or under-resolves the distribution function in velocity-space. We show that information loss is important for MMS observations.

There are a number of important consequences of the present study. First, the good agreement of kinetic entropy densities in MMS observations (in an open naturally occurring system) and PIC simulations (in a closed system) shows that closed simulations can be useful to help interpret observations in naturally occurring open systems. Second, we argue that knowledge of information loss is an important consideration for future satellite instrument development. Third, we argue that information loss is likely important in other attempts to measure non-Maxwellianity using observational data, potentially jeopardizing the accuracy of the measurement. This implies that a source of apparent irreversibility in observations is the amount of information lost by not properly resolving the distribution function.

The paper is organized as follows: Section II reviews the theoretical development of kinetic entropy, then generalizes the theory to non-uniform velocity space grids and transforms the equations to spherical energy space to be applied to satellite observations. Section III describes the in-situ data used in the study (§III A), gives an overview of the reconnection event being analyzed (§III B), and describes the PIC simulations carried out (§III C). Section IV describes our results; beginning with a Maxwellian look-up table used to minimize errors between the observed distribution and its associated Maxwellianized version needed to calculate non-Maxewllianity (§IV A); followed by a comparison between observations and PIC simulations (§IV B); and ending with a look at kinetic entropy, non-Maxwellianity, and their connection to distribution functions that represent different dissipation processes (§IV C). Section V demonstrates how course-graining velocity-space can lead to a loss of information regarding dissipation. Finally, Section VI discusses our results and Section VII presents a summary of our conclusions.

II.   KINETIC ENTROPY: THEORY

In this section, we review the theory of velocity-space kinetic entropy and non-Maxwellianity, following closely the steps outlined in Appendix A of Liang *et al.*[22], then generalize the theory to satellite applications that use non-uniform velocity space bins and require a transformation to logarithmic, spherical energy coordinates. More complete derivations of the kinetic entropy parameters, along with other quantities used or discussed throughout the paper, can be found in the supplementary material.

A.   Review of Kinetic Entropy with a Uniform Velocity Space Grid

Kinetic entropy S as defined by Boltzmann[42] is written as

$$S = k_B \ln \Omega, \tag{1}$$

where k_B is Boltzmann's constant, $\Omega = N_{tot}! / \prod_{j,k} N_{j,k}!$ is the total number of microstates that correspond to a given macrostate, N_{tot} is the total number of particles in the system, $N_{j,k}$ is the number of particles in the j, k'th cell of phase space, and the product over j and k is over all position- and velocity-space cells, respectively. We suppress writing a possible time t dependence here and throughout for simplicity. We call this form "combinatorial entropy" because of how the microstates are counted.

By breaking up phase space into discrete bins and applying Stirling's approximation, combinatorial entropy can be written in terms of the particle distribution function $f(\mathbf{r}, \mathbf{v}) = N_{j,k}/(\Delta^3 r \Delta^3 v)$ as[22,42]

$$S = k_B \left\{ N_{tot} \ln \left(\frac{N_{tot}}{\Delta^3 r \Delta^3 v} \right) - \int d^3 r \int d^3 v f(\mathbf{r}, \mathbf{v}) \ln \left[f(\mathbf{r}, \mathbf{v}) \right] \right\}. \tag{2}$$

where the small phase space cells have uniform dimensions of size $\Delta^3 r$ and $\Delta^3 v$. In writing this expression, the phase space volume has been written as infinitesimals $d^3 r d^3 v$ in the integral in the second term but remains $\Delta^3 r \Delta^3 v$ in the first term. This implies that Eq. 2 is only semi-continuous and that the finite grid size of any practical simulation or measurement device factors into the total entropy[22,24].

By considering the permutation of particles in position- and velocity-space separately, the total combinatorial entropy can be decomposed into position-space combinatorial entropy

S_r and velocity-space combinatorial entropy S_V, each of which has a semi-continuous representation similar to Eq. 2[22,43]. It is illustrative to note that the same semi-continuous forms of position- and velocity-space entropy can be derived directly from Eq. 2. After adding and subtracting $\int d^3 r n(\mathbf{r}) \ln [n(\mathbf{r})]$ and some simplification, Eq. 2 becomes

$$S = S_r + S_V \tag{3}$$

where

$$S_r = k_B \left\{ N_{tot} \ln \left(\frac{N_{tot}}{\Delta^3 r} \right) - \int d^3 r n(\mathbf{r}) \ln [n(\mathbf{r})] \right\} \tag{4}$$

$$S_V = \int d^3 r s_V(\mathbf{r}) \tag{5}$$

$$s_V(\mathbf{r}) = k_B \left\{ n(\mathbf{r}) \ln \left[\frac{n(\mathbf{r})}{\Delta^3 v} \right] - \int d^3 v f(\mathbf{r}, \mathbf{v}) \ln [f(\mathbf{r}, \mathbf{v})] \right\} \tag{6}$$

The second term in Eq. 6 is often referred to as the total kinetic entropy density $s(\mathbf{r})$,

$$s = -k_B \int d^3 v f(\mathbf{v}) \ln [f(\mathbf{v})], \tag{7}$$

where we begin to suppress the $\mathbf{r}$ dependence except where it is important to retain. This is the density of S because its position space integral gives the total kinetic entropy S in Eq. 2 (up to a constant).

For a drifting Maxwellian distribution of the form

$$f_M(\mathbf{v}) = n \left(\frac{m}{2\pi k_B T} \right)^{3/2} e^{-m(\mathbf{v} - \mathbf{u})^2 / 2k_B T}, \tag{8}$$

where m is the mass of the particles, n is the number density, $\mathbf{u}$ is the bulk flow velocity, and T is the temperature, Eq. 7 is exactly solvable, and gives the kinetic entropy density s_M of a Maxwellian distribution:

$$s_M = \frac{3}{2} k_B n \left[1 + \ln \left(\frac{2\pi k_B T}{mn^{2/3}} \right) \right]. \tag{9}$$

Substituting this into Eq. 6 gives

$$s_{M,V} = \frac{3}{2} k_B n \left[1 + \ln \left(\frac{2\pi k_B T}{m (\Delta^3 v)^{2/3}} \right) \right], \tag{10}$$

the velocity-space entropy density of a Maxwellian distribution.

Because the Maxwellian distribution describes a plasma in local thermodynamic equilibrium, and because that equilibrium state has the highest entropy of all distributions with

the same energy and number of particles[42], the difference in kinetic entropy density between an observed distribution and its associated Maxwellian, or the non-Maxwellianity of the distribution[23],

$$\bar{M}_{KP} = \frac{s_M - s}{(3/2)k_B n},$$ (11)

is a measure of the departure from Maxwellianity of a local distribution function and gives a measure for the possibility for dissipation to occur. Eq. 11 was defined by Kaufmann and Paterson[23] and is normalized by $\frac{3}{2}k_B n = c_v n$, where c_v is the specific heat per particle at constant volume for an ideal gas, to make $\bar{M}_{KP}$ dimensionless.

One disadvantage of $\bar{M}_{KP}$ is that it is not bounded, making its interpretation difficult[24]. To remedy this, a new non-Maxwellianity measure formed from the velocity-space entropy density (Eq. 6) was introduced[24]

$$\bar{M} = \frac{s_{M,V} - s_V}{s_{M,V}}.$$ (12)

Provided the velocity space grid is chosen appropriately, as discussed in Liang $et\ al.$[24], this measure is not only dimensionless, positive definite, and vanishes when the distribution is a Maxwellian (similar to $\bar{M}_{KP}$), but is also bounded. It can be written in terms of total entropy density s (Eq. 7)

$$\bar{M} = \frac{s_M - s}{s_M + k_B n \ln\left(n/\Delta^3 v\right)}$$

but we will evaluate it in terms of $\bar{M}_{KP}$ (Eq. 11)[24]

$$\bar{M} = \frac{\bar{M}_{KP}}{1 + \ln\left\{(2\pi k_B T)/\left[m\left(\Delta^3 v\right)^{2/3}\right]\right\}}.$$ (13)

because this allows us to isolate the effects that discretizing phase space has on our ability to measure entropy and non-Maxwellianity. We will explore these effects further in §V and §VI.

B.   Generalization to non-Uniform Velocity Space Grids

We now consider the velocity-space kinetic entropy and non-Maxwellianity in the context of observations by the MMS mission. The derivations in the previous subsection were performed assuming uniformly sized velocity-space bins. In practice, however, the instruments that measure the particle distribution functions, such as the Fast Plasma Investigation[44] (FPI) on MMS, have logarithmically-spaced energy bins, meaning $\Delta^3 v$ is not a constant and

cannot be pulled out of the summation that leads to the first term in Eqs. 2 and 6. We now follow the same procedure as for Equations 1-6, deriving the combinatorial form of S_r and S_V but with the velocity-space bin size represented by Δv_k to indicate it is different for every velocity-space cell. Focusing on the velocity-space entropy, we obtain

$$
\begin{aligned}
S_V = \sum_j k_B \Big\{ & n(r_j)\Delta^3 r \ln \left[n(r_j)\Delta^3 r \right] \\
& - \sum_k \left(f(r_j, v_k)\Delta^3 r \Delta^3 v_k \ln \left[f(r_j, v_k) \right] \right) \\
& - \sum_k \left[f(r_j, v_k)\Delta^3 r \Delta^3 v_k \ln \left(\Delta^3 r \Delta^3 v_k \right) \right] \Big\}.
\end{aligned}
\tag{14}
$$

Now we split the $\Delta^3 r \Delta^3 v_k$ pairs, bringing the constant $\Delta^3 r$ outside of the summations, let $S_V = \sum_j s_V \Delta^3 r$, and take the limit of small velocity-space bin sizes to get

$$
s_V = s + k_B n \ln n - k_B \int d^3 v(\mathbf{v}) f(\mathbf{v}) \ln \left[d^3 v(\mathbf{v}) \right],
\tag{15}
$$

where we write an explicit dependence of $d^3 v$ on $\mathbf{v}$, and s is the entropy density from Eq. 7 with $d^3 v$ replaced by $d^3 v(\mathbf{v})$. This is the generalization of Eq. 6 for the case of non-uniform velocity bins. From here onward, when we are developing the theory, the velocity-space element will be referred to as $d^3 v(\mathbf{v})$, but for discussions of the theory, which applies to satellite instrumentation, we will refer to it as $\Delta^3 v_k$. If $\Delta^3 v_k$ were constant, it could be pulled out of the integral and the resulting $-n \ln(\Delta^3 v)$ combines with the second term to recover Eq. 6.

To calculate $\bar{M}$, we replace $\Delta^3 v$ with $\Delta^3 v_k$ in Eq. 10, take the limit of small bin size, substitute the result and Eq. 15 into Eq. 12, then simplify to get

$$
\bar{M} = \frac{s_M - s - k_B \int d^3 v(\mathbf{v}) \ln \left[d^3 v(\mathbf{v}) \right] \left[f_M(\mathbf{v}) - f(\mathbf{v}) \right]}{s_M + k_B n \ln n - k_B \int d^3 v(\mathbf{v}) \ln \left[d^3 v(\mathbf{v}) \right] f_M(\mathbf{v})}.
\tag{16}
$$

Substituting Eq. 9 into the denominator and factoring out $\frac{3}{2} k_B n$ gives

$$
\bar{M} = \frac{\bar{M}_{KP} - 2/(3n) \int d^3 v(\mathbf{v}) \ln \left[d^3 v(\mathbf{v}) \right] \left[f_M(\mathbf{v}) - f(\mathbf{v}) \right]}{1 + \ln \left(2\pi k_B T/m \right) - 2/(3n) \int d^3 v(\mathbf{v}) \ln \left[d^3 v(\mathbf{v}) \right] f_M(\mathbf{v})}
\tag{17}
$$

Note that the densities of $f(\mathbf{v})$ and $f_M(\mathbf{v})$ are equal by definition. This means that if $\Delta^3 v_k$ were constant, the final term in the numerator of Eq. 17 would vanish and the third term in the denominator would reduce to $-\ln(\Delta^3 v)^{2/3}$, which recovers Eqs. 11 and 12.

Kinetic Entropy in an EDR

The prior expressions are valid regardless of the velocity space grid sizes. Here, we derive expressions for spherical energy space coordinates that particle detectors use. For the case of MMS-FPI, an additional step is needed; the particle energy E is normalized via

$$U = \frac{E}{E_0 + E},\tag{18}$$

where E_0 is a constant used to bound the energy integration limits of the distribution function between 0 and 1 (more on this in §III A). To perform the coordinate transformations, we assume a non-relativistic system and follow the notation of Moseev and Salewski[45]. First, we establish the relationship between v, E, and U:

$$v = \sqrt{\frac{2E}{m}} \qquad\qquad dv = \frac{dE}{\sqrt{2mE}}$$

$$v = \sqrt{\frac{2E_0}{m}}\sqrt{\frac{U}{1-U}} \qquad\qquad dv = \sqrt{\frac{E_0}{2m}}\frac{dU}{\sqrt{U}(1-U)^{3/2}}$$

$$E = \frac{E_0 U}{1-U} \qquad\qquad dE = \frac{E_0}{(1-U)^2}dU.$$

Next, we find the Jacobians of the transformations as

$$J_{v_x,v_y,v_z \to \phi,\theta,v} = \det\left|\frac{\partial(v_x,v_y,v_z)}{\partial(\phi,\theta,v)}\right| = v^2 dv d\Omega \tag{19}$$

$$J_{v_x,v_y,v_z \to \phi,\theta,E} = \det\left|\frac{\partial(v_x,v_y,v_z)}{\partial(\phi,\theta,E)}\right| = \frac{\sqrt{2}}{m^{3/2}}\sqrt{E}dE d\Omega \tag{20}$$

$$J_{v_x,v_y,v_z \to \phi,\theta,U} = \det\left|\frac{\partial(v_x,v_y,v_z)}{\partial(\phi,\theta,U)}\right| = \sqrt{2}\left(\frac{E_0}{m}\right)^{3/2}\frac{\sqrt{U}}{(1-U)^{5/2}}dU d\Omega, \tag{21}$$

where $d\Omega = \sin\theta d\theta d\phi$ is an element of solid angle in velocity space, and ϕ and θ are the azimuth and polar angles, respectively.

These relationships can then be used to transform the kinetic entropy equations into spherical, normalized energy coordinates. Starting with the Maxwellian distribution (Eq. 8):

$$f_M(\phi,\theta,U) = \frac{n}{(\pi k_B T)^{3/2}}\left(\frac{m}{2}\right)^3\frac{E_0 U}{1-U}\exp\left[\frac{-\left(\sqrt{\frac{E_0 U}{1-U}}\sin\theta\cos\phi - \sqrt{\frac{1}{2}m}u_x\right)^2}{k_B T}\right]$$

$$\exp\left[\frac{-\left(\sqrt{\frac{E_0 U}{1-U}}\sin\theta\sin\phi - \sqrt{\frac{1}{2}m}u_y\right)^2}{k_B T}\right]\tag{22}$$

$$\exp\left[\frac{-\left(\sqrt{\frac{E_0 U}{1-U}}\cos\theta - \sqrt{\frac{1}{2}m}u_z\right)^2}{k_B T}\right]$$

where f_M has been written such that $n = \int f_M dU d\Omega$. Next, we do the same for Equations 7, 15, 16, and 17 to get:

$$s = -k_B \sqrt{2} \left(\frac{E_0}{m} \right)^{3/2} \int \frac{\sqrt{U}}{(1-U)^{5/2}} f(\phi, \theta, U) \ln \left[f(\phi, \theta, U) \right] dU d\Omega \tag{23}$$

$$\begin{aligned} s_V = &s + k_B n \ln \left[\frac{n}{\sqrt{2}} \left(\frac{m}{E_0} \right)^{3/2} \right] \\ &- k_B \sqrt{2} \left(\frac{E_0}{m} \right)^{3/2} \int \frac{\sqrt{U}}{(1-U)^{5/2}} \ln \left[\frac{\sqrt{U}}{(1-U)^{5/2}} dU d\Omega \right] f(\phi, \theta, U) dU d\Omega \end{aligned} \tag{24}$$

$$\bar{M} = \frac{s_M - s - \mathcal{E}_0 k_B \int \mathcal{U} dU d\Omega \ln (\mathcal{U} dU d\Omega) \left[f_M(\phi, \theta, U) - f(\phi, \theta, U) \right]}{s_M - k_B n \left[\ln n - \mathcal{E}_0 \ln (\mathcal{E}_0) \right] - \mathcal{E}_0 k_B \int \mathcal{U} dU d\Omega \ln (\mathcal{U} dU d\Omega) f_M(\phi, \theta, U)} \tag{25}$$

$$\bar{M} = \frac{\bar{M}_{KP} - \frac{1}{3n} \left(\frac{2E_0}{m} \right)^{3/2} \int \frac{\sqrt{U}}{(1-U)^{5/2}} \ln \left[\frac{\sqrt{U}}{(1-U)^{5/2}} dU d\Omega \right] \left[f_M(\phi, \theta, U) - f(\phi, \theta, U) \right] dU d\Omega}{1 + \ln \left(\frac{2^{2/3} \pi k_B T}{E_0} \right) - \frac{1}{3n} \left(\frac{2E_0}{m} \right)^{3/2} \int \frac{\sqrt{U}}{(1-U)^{5/2}} \ln \left[\frac{\sqrt{U}}{(1-U)^{5/2}} dU d\Omega \right] f_M(\phi, \theta, U) dU d\Omega}. \tag{26}$$

We made the substitutions $\mathcal{E}_0 = \sqrt{2} \left(\frac{E_0}{m} \right)^{3/2}$ and $\mathcal{U} = \frac{\sqrt{U}}{(1-U)^{5/2}}$ in Eq. 25 to save space and we continue to suppress the dependence of the distribution function on $\mathbf{r}$. An additional note is that if the roles of $\mathbf{v}$ and $\mathbf{r}$ were switched, one could arrive at a position-space entropy density that is local in velocity space and its equivalent expression for non-Maxwellianity. We do not pursue this line of thought on practical grounds.

III. DATA

A. MMS

Kinetic entropy and non-Maxwellianity are explored using data from the Dual Electron Spectrometer (DES) from the Fast Plasma Investigation (FPI)[44] on the MMS mission[16]. DES measures the full 3D electron distribution function every 30 ms in burst mode. We integrate the distribution using the new theory of §II B to calculate kinetic entropy parameters. For consistency in results (e.g., calculations of s_M using Eq. 9 vs. Eq. 7 with Eq. 8), we perform our own numerical integration of the distribution function for both the kinetic entropy parameters and the plasma moments using the method prescribed by the FPI team. This involves 1) removing photoelectrons generated by sunlight entering the instrument aperture, 2) correcting for the spacecraft potential that acts as a barrier to cold particles

and changes the energy of incoming plasma, and 3) preconditioning the distribution, which entails normalizing the energy range according to Equation 18 and extrapolating the ϕ, θ, and U integration limits so that ϕ is cyclic, θ ranges from $[0, \pi]$, and U ranges from $[0, 1]$. The value of E_0, conditions for energy extrapolation, and energy integration limits are provided in the metadata of the official DES moments files available through the MMS Science Data Center[46]. Finally, trapezoidal integration is performed in spherical, normalized energy coordinates.

In addition to DES data, we also make use of the FIELDS instrument suite[47], which contains the Fluxgate Magnetometer (FGM)[48] and the Electric Field Double Probes (EDP)[49,50] instruments that measure the magnetic and electric fields, respectively. Vector data is displayed in the LMN boundary normal coordinate system obtained via a minimum variance analysis of the electron bulk velocity (MVA-V_e) within the EDR[51,52]. In this system, $\hat{e}_L$ points along the Earthward exhaust, $\hat{e}_N$ points North toward the inflow region, and $\hat{e}_M = \hat{e}_N \times \hat{e}_L$ points along the reconnecting current. This coordinate system results in a reliable reconnection rate[52].

B. Event Overview

Measurements from July 11, 2017, around 22:34:00 Universal Time (UT), are shown in Figure 1. The MMS satellites[16] were embedded in the central magnetotail plasma sheet, as indicated by the hot, dense ion and electron populations in Figure 1b,c,d. As MMS3 traversed the plasma sheet from the Southern to the Northern hemisphere, it observed a rotation of the reconnecting magnetic field B_L (Fig. 1a), a reversal of an ion jet $V_{i,L}$ (Fig. 1e), and a reversal of an electron jet $V_{e,L}$ (Fig. 1f), indicating that MMS crossed from the earthward to the tailward exhausts of a reconnection site. Hall electric fields E_N (Fig. 1g) signal the separation of charge within the ion diffusion region. The strong out-of-plane electron flow $V_{e,M}$ co-incident with the electron jet reversal was found to be caused by accelerated, meandering electrons accelerated by the reconnection electric field E_M in the EDR. The EDR is further identified by the departure of the perpendicular electron bulk flow from the ExB drift velocity, indicating a violation of the frozen-in condition[39]. Farther into the tailward exhaust, MMS encountered electron-scale vortices[53] within ion-scale flux ropes[53,54] (not shown) associated with a turbulent exhaust structure.
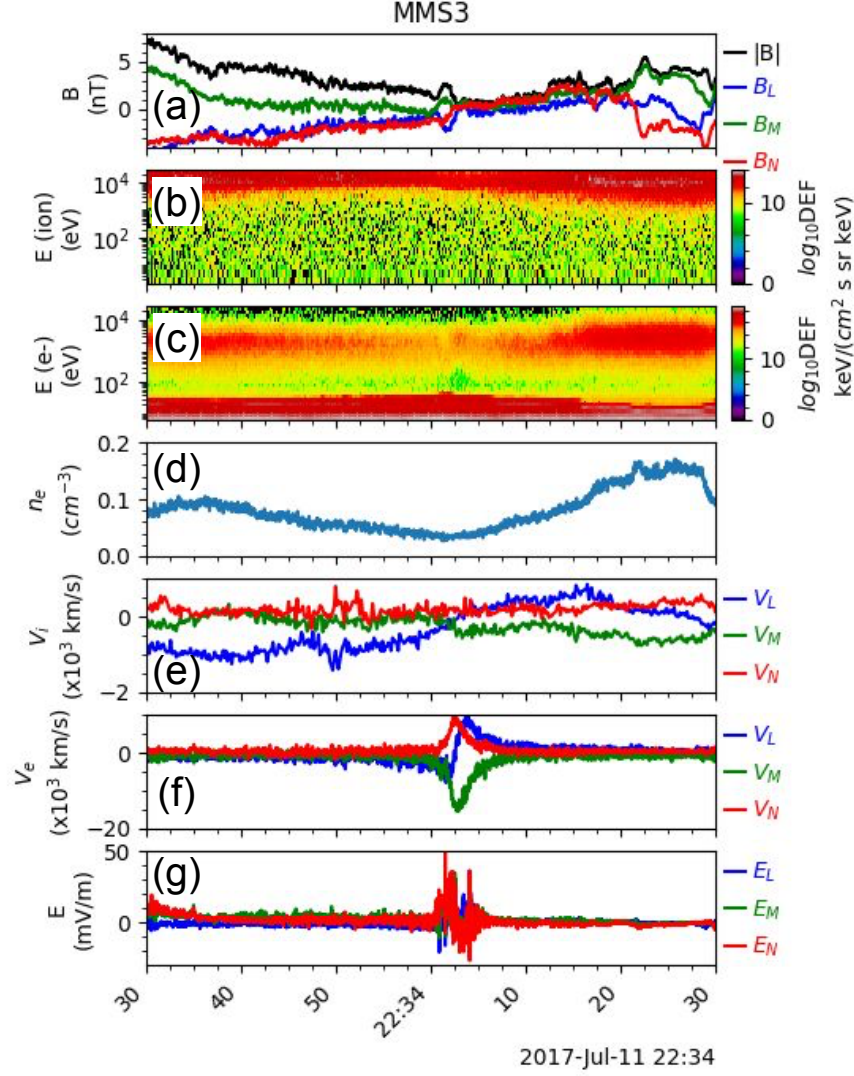
FIG. 1. MMS encounter with an electron diffusion region[39]. (a) Magnetic field components and magnitude, (b) ion and (c) electron energy spectrograms, (d) electron number density, (e) ion and (f) electron bulk velocity, and (g) electric field components. Data is shown in the LMN-coordinate system of Nakamura et al.[55]

The EDR for this event has been studied extensively. Some of the primary conclusions from previous studies were that this symmetric magnetotail reconnection event with weak guide field is characterized by a 2D, laminar process[39,51], the normalized reconnection rate was 0.1-0.22[39,52,55,56], the structure of the X-line is supported by electron nongyrotropy[51,56,57], and electrons are accelerated to super-Alfvénic velocities after spending at least three gyroperiods in the current sheet[39]. In addition, Torbert et al.[39] describes a ×2 calibration

13

factor that has been applied to the ion velocities in Figure 1e. For more detailed analysis of this event, readers are referred to the cited papers.

C.   Simulation

The observed reconnection event was nearly symmetric and reasonably laminar, and previous studies employing 2.5D PIC simulations have shown good agreement with the observations[39,51,55,57]. We therefore also employ 2.5D PIC simulations to compare with the observations. We use the massively parallel PIC code P3D[58], where particles are stepped forward in time using the relativistic Boris particle stepper[59] and electromagnetic fields are stepped forward using the trapezoidal leapfrog method[60]; the fields can have a smaller time-step than that of the particles. P3D employs the multigrid approach to clean the electric field, $\mathbf{E}$, to enforce $\nabla \cdot \mathbf{E} = \rho/\epsilon_0$, where ρ is the net charge density, every 10 particle time-steps. We employ periodic boundary conditions in both directions with a large enough computational domain that the boundaries are not expected to play much of a role in the region of interest at the time examined. A motivation for choosing periodic boundary conditions over open ones is to see if the local kinetic entropy densities obtained in a closed system are representative of the local kinetic entropy obtained in the (open) real system.

The initial setup of the simulation has two Harris current sheets (CS) and a uniform background (BG) plasma population for which the density n_{BG} and temperature $T_{s,BG}$ for species s (either e for electrons or i for ions) can be chosen independently from the Harris sheet parameters. The initial magnetic field profile is $B_L(N) = B_0[\tanh\left[(N - l_N/4)/w_0\right] - \tanh\left[(N - 3l_N/4)/w_0\right] - 1]$, where B_0 is the asymptotic reconnecting magnetic field far upstream, w_0 is the half-thickness of the current sheet and l_N is the width of the computational domain in the $\hat{e}_N$ direction. Initially, the electrons and ions in the Harris sheets have the same density profile, $n_{CS}(N) = n_0 \left(\mathrm{sech}^2\left[(N - l_N/4)/w_0\right] + \mathrm{sech}^2\left[(N - 3l_N/4)/w_0\right]\right)$, where $n_0 = B_0^2/[8\pi k_B(T_{e,CS}+T_{i,CS})]$ and $T_{s,CS}$ are the temperatures of the current sheet population for each species.

For the plasma parameters in the simulations, we employ the same values used by Nakamura et al.[55] The upstream (lobe) magnetic field is $B_0 = 12\,\mathrm{nT}$ and the density at the center of the initial CS is $n_0 = 0.0896\,\mathrm{cm}^{-3}$. The electron CS temperature $T_{e,CS} = 1.053\,\mathrm{keV} = 0.125\,T_0$ and ion CS temperature $T_{i,CS} = 3\,T_{e,CS}$, where $T_0 = m_i V_{Ai0}^2/k_B = 8.424\,\mathrm{keV}$ and

$V_{Ai0} = 875\,\text{km/s}$ is the Alfvén speed based on n_0 and B_0. The background (lobe) electron temperature $T_{e,BG} = 0.351\,\text{keV} = 0.04167\,T_0$ and the background ion temperature $T_{i,BG} = 3\,T_{e,BG}$. The BG density is $n_{BG} = 0.0296\,\text{cm}^{-3} = 0.33\,n_0$. These parameters result in an upstream electron Debye length of $\lambda_{De} = 0.018d_{i0} = 1.37 \times 10^4\,\text{m}$, and upstream total beta of $\beta = 0.11$.

The speed of light c is $1.75 \times 10^4\,\text{km/s}$ which is smaller than that of Nakamura $et\ al.$[55] but is sufficiently larger than other speeds of our system. The initial current sheet half-thickness $w_0 = 456\,\text{km} = 0.6\,d_{i0}$, where $d_{i0} = c/\omega_{pi0} = 760\,\text{km}$ is the ion inertial length based on n_0, $\omega_{pi0} = (n_0 e^2/\epsilon_0 m_i)^{1/2}$ is the ion plasma frequency, and e is the proton charge, which is the same as in Nakamura $et\ al.$[55]. The electron to ion mass ratio is $m_e/m_i = 0.01$ which is larger than in Nakamura $et\ al.$[55] and is a factor of 18.36 larger than the realistic value. This means the electron-to-ion inertial length ratio in the simulations is a factor of 4.28 larger than the realistic length ratio. This difference will be noted while drawing comparisons between observation and simulation results, but we do not expect that electron scale properties of the reconnection region are altered when properly normalized to a realistic value.

The length of the computational domain is $l_L = 2.66 \times 10^4\,\text{km} = 35\,d_{i0}$ and its width is $l_N = 1.33 \times 10^4\,\text{km} = 17.5\,d_{i0}$. The system size is smaller than that of Nakamura $et\ al.$[55] but since the focus of our study is a trajectory which passes very close to the electron diffusion region, a smaller system size is sufficient; our system size is not large enough for ions to fully couple to the reconnected field downstream of the X-point, but this is not expected to affect dynamics at the electron scale that are the focus of this study. The grid-length Δ in both directions $= 6.5\,\text{km} = 0.008545\,d_{i0}$, which is chosen to be smaller than the smallest length scale of the system (the electron Debye length). The time-step $\Delta t = 0.652\,\text{ms} = 0.00075\,\Omega_{ci0}^{-1}$ is chosen to be smaller than the smallest time scale of the system (the electron plasma frequency), where Ω_{ci0} is the ion cyclotron frequency based on B_0. The time step for electromagnetic fields is half of that for the particles. There are 4096×2048 grid cells which are initialized with 100 weighted particles per grid (PPG). To initiate reconnection, an X point/O point pair are seeded in both current sheets using a weak magnetic field perturbation of the form $\delta B_L = -0.08 B_0 \sin\left(2\pi L/l_L\right)\sin\left(4\pi N/l_N\right)$ and $\delta B_N = 0.08 B_0 [l_N/(2l_L)]\cos\left(2\pi L/l_L\right)[1 - \cos\left(4\pi N/l_N\right)]$.

Kinetic entropy is calculated in the simulations employing the implementation from Liang $et\ al.$[22] with one noteworthy difference. The velocity-space grid scale Δv_i for ions and Δv_e

for electrons was imposed to be equal to each other in previous works[22,24]. In the present study, we allow Δv_i and Δv_e to be chosen independently. Moreover, this study employs two populations in the initial Harris sheet profile, compared to a single drifting Maxwellian distribution in previous works. Therefore, we optimize the velocity-space grid scale analogously to the previous works, but specifically check the agreement between kinetic entropy density calculated by the simulation and the theoretical value in both the background plasma and the current sheet center simultaneously. We calculate the kinetic entropy density for each species in the simulations with varying velocity-space grids in order to find the optimal velocity-space grid scale at $t = 0$. This is an important step because if the velocity space grid is too small, the distribution is over-resolved, meaning there is not a statistically significant number of particles per grid cell. Meanwhile, if the grid size is too large, the distribution is under-resolved and important structures are lost. (See §V for a detailed explanation.) The kinetic entropy density for either species is given by Eq. 7 with $f = f_{CS} + f_{BG}$, consisting of both the current sheet and background populations at $t = 0$. Since these integrals cannot be done analytically, we carry out these integrals numerically. After we choose a (Cartesian) velocity-space grid scale for electrons, we numerically compute the entropy and compare it to the theoretical value. This results in agreement to within $\pm 1\%$ in the upstream region and $\pm 2\%$ at the center of the current sheet. The optimal velocity-space grid scale for each species is $60 - 65\%$ of the smaller of the background and current sheet thermal speeds. For electrons, each velocity-space direction is binned from $(-1.67, 1.67) \times 10^4 \, \mathrm{km/s}$ =(-18.71, 18.71) V_{Ai0} with 22 bins of size $\Delta v_e = 1.48 \times 10^3 \, \mathrm{km/s}{=}1.7005 \; V_{Ai0}$. For ions, the binning range is $(-7.34, 7.34) \times 10^3 \, \mathrm{km/s}{=}$(-8.38, 8.38) V_{Ai0} with 54 bins with bin-size $\Delta v_i = 2.72 \times 10^2 \, \mathrm{km/s}{=}0.3105 \, V_{Ai0}$.

Previous simulation studies[22,24] employed a look-up table similar to the one discussed in §IV A to calculate the Maxwellianized entropy s_M. A look-up table for the simulation is advantageous because the simulated plasma has PIC noise while the analytical expression does not. Using raw density and temperature values with an analytical expression for the Maxwellianized entropy leads to disagreement with the theoretical value. The look-up table allows comparable amounts of error in the simulated and theoretical values, which improves the agreement with theory.

For the present study, we find that unlike in Liang *et al.*[24], the results for s_M when using a look-up table are significantly different than when not using one. The reason for the dis-

agreement is mixing between macroparticles of different numerical weight; previous studies employed a look-up table that assumed the weights were the same for all macroparticles. As macroparticles of different weight mix, the look-up table becomes less accurate. This could be addressed by including a third axis of the look-up table to incorporate particle weight, but that is not undertaken for the present study. We therefore directly calculate s_M to get simulated values of the non-Maxwellianity parameters.

The simulation results we present are carried out with no initial out of plane (guide) magnetic field B_g. It is important to put this choice in the context of previous numerical simulations of the observed event that employed a weak initial guide field[55,57]. We perform and compare results from test simulations with and without a weak initial guide field of $B_g = -0.36$ nT $= -0.03 B_0$. Figure 2 shows 2D plots of the out-of-plane magnetic field component B_M, where the X-line is located at $(0,0)$ and the separatrices are the black curves. In the presence of the weak guide field (Fig. 2a), we find that B_M has a value of about -0.6 nT $= -0.05\, B_0$ in the vicinity of the EDR. This is not seen in MMS3 data (see Figure 4e; B_M does not become appreciably negative in the shaded region). In our simulations without an initial guide field (Fig. 2b) we find that B_M is again negative in the vicinity of the X-line along the virtual spacecraft trajectory marked by the thick black curve, but has a smaller value of -0.24 nT $= -0.02 B_0$, closer to the MMS3 observations. We find no comparable virtual trajectory in the simulation with an initial guide field that reproduces the signature of B_M observed by MMS3, so we use the $B_g = 0$ simulation for this study. Egedal *et al.*[57] also used a guide field weaker than that of Nakamura *et al.*[55] for similar reasons.

Finally, we note that the virtual spacecraft trajectory is selected from a set of possible trajectories, chosen by eye (as opposed to using more systematic approaches to determine the trajectory[51,57,61]). The selected trajectory is one which produces qualitatively similar trends of magnetic field and electron flow speeds when compared with MMS3 observations. We do not anticipate significantly different values by employing more systematic approaches. In what follows, all plots are made from the lower current sheet at the simulation time of $23.4\,\mathrm{s} = 27\,\Omega_{ci0}^{-1}$, when the system has achieved a steady-state reconnection rate (not shown).
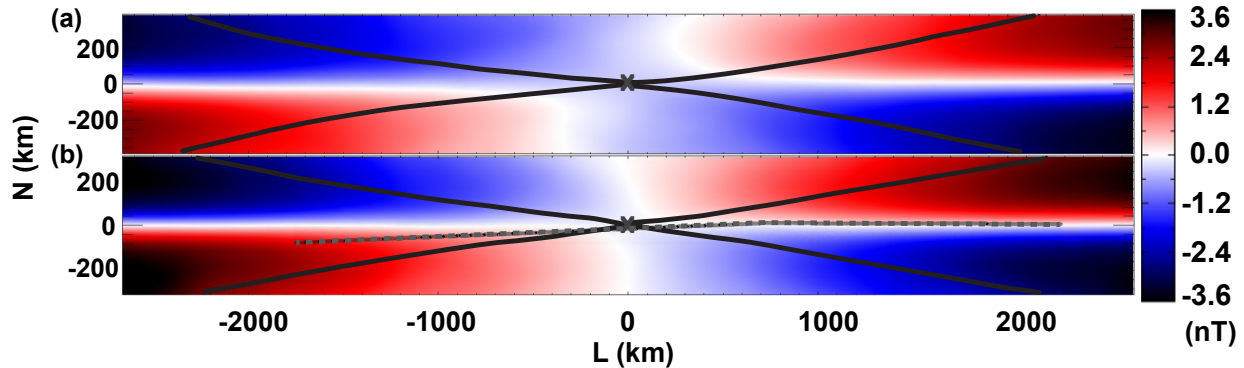
FIG. 2. Out of plane magnetic field B_M from simulations (a) with and (b) without an initial guide field of $B_g = -0.36$ nT $= 0.03B_0$. The separatrices are thick black curves and the thick black line in (b) is our selected virtual spacecraft trajectory.

IV.   RESULTS

A.   Maxwellian Look-up Table

In order to compute the non-Maxwellianity of a measured distribution $f(\mathbf{v})$, it must be compared to its associated Maxwellian —a Maxwellianized distribution $f_M(\mathbf{v})$ of the form Eq. 8 with the same density and temperature as the measured distribution $f(\mathbf{v})$. (The bulk velocity need not be calculated because it does not factor into Eqs. 6 or 7.) For a continuous, analytical function, the density and temperature of $f_M(\mathbf{v})$ are defined to be equal to those of $f(\mathbf{v})$. However, the distribution function $f(\phi, \theta, E)$ measured by particle instruments is discrete, not continuous, and is in spherical energy coordinates, not Cartesian velocity coordinates. These differences introduce numerical errors into calculations involving the distribution function. Namely, the computed value of the Maxwellian kinetic entropy density, s_M, can be less than the kinetic entropy density calculated directly from MMS data, s. Given that s_M is the maximum entropy density for a fixed number of particles and total energy, $s_M < s$ is unphysical..

To create a Maxwellianized distribution, we write f_M (Eq. 8) in spherical velocity coordinates. We then calculate $f_M(\phi, \theta, v)$ at the same azimuth, polar, and velocity bin centers as FPI and transform it to $f_M(\phi, \theta, U)$ using the steps outlined in §III A. In this way, the Maxwellian distribution is treated the same as the measured distribution. The result is Equation 22.

Numerical errors between the measured distribution and its associated Maxwellian prompted us to create a Maxwellian look-up table for the MMS observations. We start by determining the range of observed densities and temperatures for the event. Then, we create our look-up table coordinates n_{lut} and T_{lut} on a 2D grid in density- and temperature-space that spans the observed ranges. For each value of n_{lut} and T_{lut} in the look-up table, we use a Monte Carlo approach to generate a Maxwellian distribution governed by Eq. 22 with $\mathbf{u} = 0$, giving $f_M(\phi, \theta, U)$ at each n_{lut}, T_{lut}. This constitutes the Maxwellian look-up table. We note, however, that for any $f_M(\phi, \theta, U)$ in the look-up table, its numerically integrated density n_M and temperature T_M are not necessarily equal to the n_{lut} and T_{lut} used to produce it due to the coordinate transformations, discretization, and extrapolation that f_M underwent.

Figure 3 shows the percent error in (a) density $\Delta n/n = (n_{lut} - n_M)/n_{lut} \times 100\%$ and (b) temperature $\Delta T/T = (T_{lut} - T_M)/T_{lut} \times 100\%$ as a function of the look-up table coordinate T_{lut} during the EDR encounter on 2017-07-11[39] (§III B, Fig. 1). Errors in both density and temperature are independent of density. Absolute errors in density are greater than 6.4% for low temperatures and decrease monotonically and non-linearly to 1.9% with increasing temperature. Similarly, absolute errors in temperature reach a maximum of 2.9% at 400 eV then decrease non-linearly to 1.1% at the upper limit of the temperature range. The negative (positive) sign on the relative errors for density (temperature) indicates that the Maxwellianized distribution consistently has a higher density and lower temperature than the look-up density and temperature.

Adjustments in the look-up table method reduce the errors between the observed and associated Maxwellian parameters. During the EDR encounter, the observed density and temperature are used to look up the associated errors from Figures 3a,b, which are then plotted as a function of time in Figures 3c,d (blue). To reduce the errors, instead of selecting f_M at the grid point (n_{lut}, T_{lut}) that is closest to the observed values (n, T), we select f_M at the grid point (n'_{lut}, T'_{lut}) that minimizes $\sqrt{(\Delta n/n)^2 + (\Delta T/T)^2}$. These adjusted results are plotted in orange. While still noisy, the adjusted look-up values for n_M and T_M result in errors that are on average zero.

The effect of these adjustments on measures of kinetic entropy are shown in Figures 3e,f. Because the Maxwellian distribution has the highest entropy of any distribution with the same total number of particles and internal energy, it should be true that $\Delta s/s \leq 0$ and
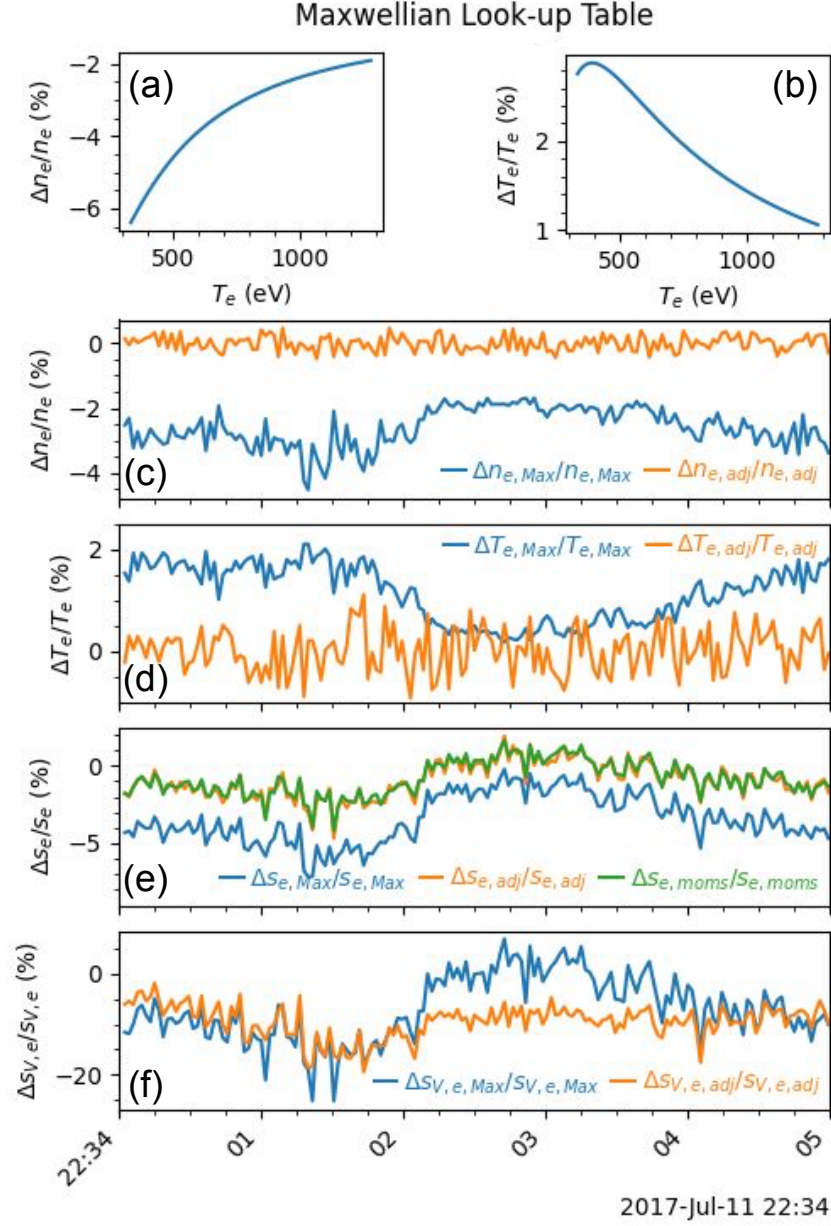
FIG. 3. Maxwellian look-up table illustrating the numerical errors introduced by coordinate system transformations and how it is used to correct for those errors. (a) Density and (b) temperature look-up tables relating the observed density and temperature to those of the equivalent Maxwellian distribution. The error as a function of time during the period of interest for (c) density, (d) temperature, (e) entropy density, and (f) velocity space entropy density without (blue) and with (orange) using the look-up table. Look-up table results are validated by calculating the total entropy analytically using Eq. 9 (the green curve in panel e).

$\Delta s_V/s_V \leq 0$. This is the case for $\Delta s/s$ but not for $\Delta s_V/s_V$. After adjusting the look-up table method (orange curves), $\Delta s_V/s_V \leq 0$ at all times, but $\Delta s/s > 0$ at times near 22:34:03. Both s and s_V were calculated by integrating $f(\phi, \theta, U)$ and $f_M(\phi, \theta, U)$ using Eqs. 23 and 24. We also compute s_M via Eq. 9 using n and T from the official FPI moments and compare it to the observed s. This is the green curve in Figure 3e; it matches with our adjusted values of $\Delta s/s$, which serves as validation of our methodology. The reason s gives unphysical values is because, unlike s_V, s does not contain information about the velocity space grid scale. This is just one of several reasons[24] that s_V is a better choice for studying kinetic entropy; we will discuss this further in §V.

B. Comparison between Observations and the PIC Simulation

Figure 4 shows a comparison between observations (left) and the PIC simulation (right) in the same format as Figure 7 of Nakamura *et al.*[55] MMS3 passed closest to the reconnection X-line and its data is plotted during the 5 second interval starting at 22:34:00 UT because this is the time interval surrounding the EDR most commonly shown in previous studies[39,51,52,55,56]. In this study, we focus on the electron entropy in and immediately surrounding the EDR in the subinterval from $1.95\,\mathrm{s}$ to $3.315\,\mathrm{s}$, which is highlighted by the gold box in the MMS panels. Since the structure velocity is $V_L = -170\,\mathrm{km/s}$ and the electron inertial length is $d_e = 30\,\mathrm{km}$[39], the spacecraft traversed a distance of $7.7\,d_e$ during this time.

The corresponding path of the virtual spacecraft trajectory through the simulation is $5.3\,d_{i0} = 30.64\,d_e$ long, where (no) subscript 0 indicates that the (current sheet density, n_0) upstream density was used. This would correspond to a path length of $7.1\,d_e$ in a simulation with a realistic mass ratio (with m_e 18.36 times lighter), which is nearly the same as the path length in the observations. The data is taken at a single time after the simulation has reached a steady state. We include simulation results both in normalized units (left vertical axis) and physical units (right vertical axis), the latter of which allows for a quantitative comparison with the MMS data.

Quantitatively, the density (Fig. 4a,b); electron temperature anisotropy $A = T_{e,\parallel}/T_{e,\perp} - 1$, where $T_{e,\parallel}$ and $T_{e,\perp}$ are the electron temperatures parallel and perpendicular to the magnetic field (Fig. 4c,d); and magnetic field (Fig. 4e,f) are similar between observations and the simulation. The electron bulk flow (Figure 4g,h) has similar structure but is smaller in

the simulation by about a factor of 4; this is because the simulated electron mass is 18.36 times larger than the realistic value, so the electron Alfvén speed is 4.28 times smaller. The electric field components in the simulation reference frame $\mathbf{E}$ and in the electron rest frame $\mathbf{E}'$ (Fig. 4i-n) all have similar profiles to the observations, but the L and N components are about 2 times smaller in amplitude in the simulations than in the observations. Similarly, the rate of energy conversion between the electric field and the electrons (Fig. 4o,p) is a factor of about 4 lower in the simulations. We note that there is good agreement in the normalized simulation values and those presented in Nakamura *et al.*[55] (see their Figure 7), so the quantitative differences with the observations seen here are consistent with previous studies. The overall agreement between the simulation and observations gives us confidence in our comparison and interpretations of entropy that follow (§IV C).

Some differences in density visible in Figure 4a,b can be attributed to the trajectory of the virtual spacecraft through the simulation EDR. Along the trajectory, the density profiles both increase, but the simulation profile exhibits a local minimum not present in the observations. The density profile along a vertical cut through the EDR has a double peak with the peaks appearing just upstream of the X-line at the turning points of the meandering motion[62]. If our virtual trajectory began closer to, but still below, the central current sheet and sloped gently downward, the density profile would gradually increase as in the observations. However, the qualitative agreement between the fields and flows just described would suffer. We choose to keep this trajectory because of the importance of $\mathbf{B}$ and $\mathbf{V}_e$ to reconnection. We will revisit this issue when comparing entropy in the next section.

C.   Kinetic Entropy: Application

We now compare observations and simulation results of kinetic entropy parameters along the satellite trajectory to a) determine if local kinetic entropy measurements in a large, open system can be interpreted in a similar manner to those of a closed system and b) draw a link between kinetic entropy and the dissipation processes of reconnection. Figure 5 again shows the virtual satellite trajectory through the simulation domain during the gold highlighted interval, as well as a 2D snapshot of $\bar{M}$ from Eq. 12. We then plot total and velocity-space entropy densities s and s_V along with their associated Maxwellianized values s_M and $s_{M,V}$,
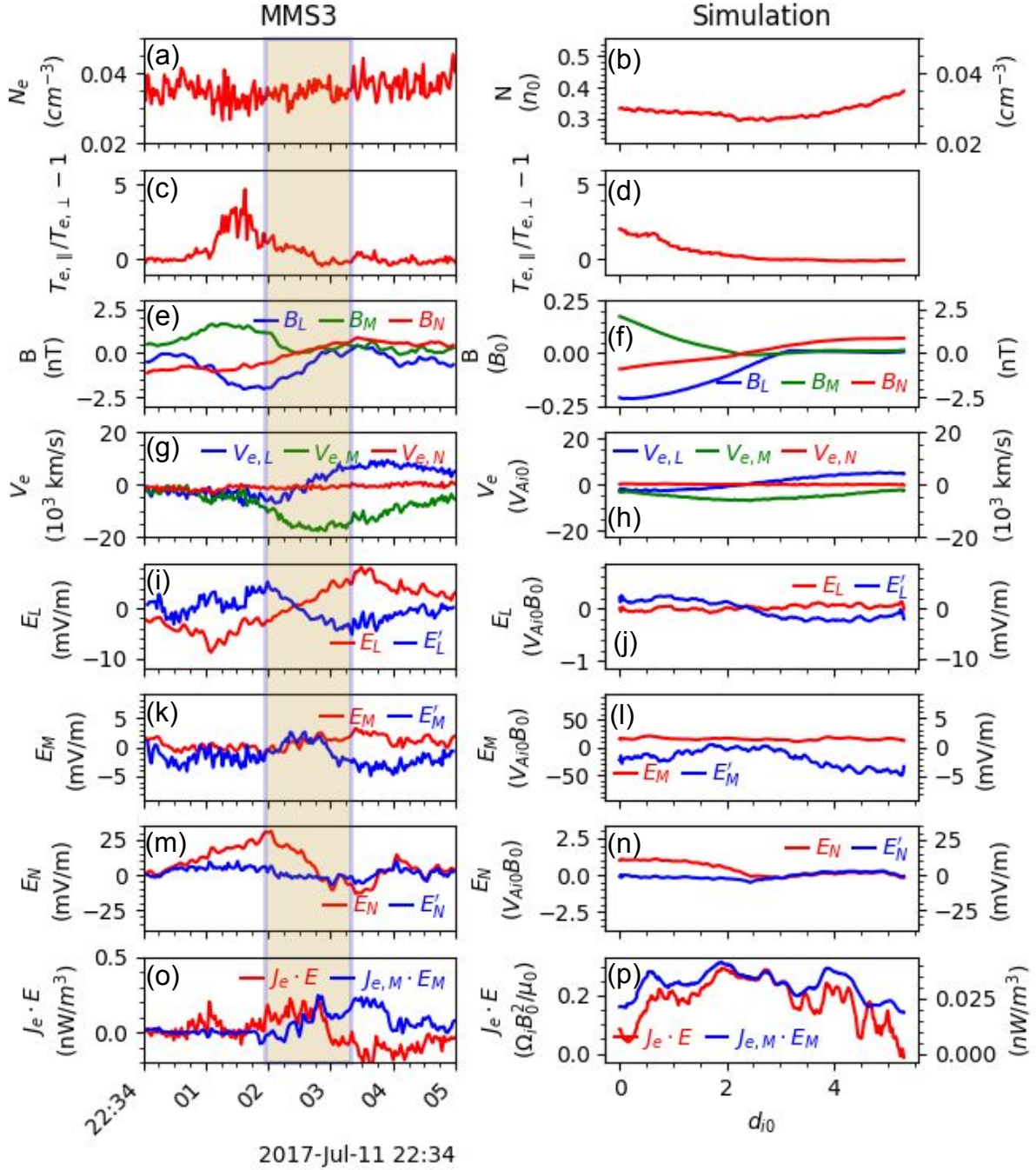
FIG. 4. Comparison between MMS observations (left) and a PIC simulation (right) of a magnetotail EDR encounter. MMS observations are shown over an extended region to provide context and comparison to previous results (see text). The gold rectangle highlights the EDR and region of overlap with simulation. Comparisons are made between (a,b) electron density, (c,d) electron temperature anisotropy, (e,f) magnetic field, (g,h) electron bulk velocity, (i-n) electric field in the spacecraft and electron rest frame, (o,p) total and M-component of the rate of energy conversion between the electric field and the electrons. Simulation data is shown in real units (right-axis) on the same scale as MMS observations with the exception of panel (p), which is much smaller in magnitude. Overall, observations and simulations are in qualitative agreement.

and the non-Maxwellianity measures $\bar{M}$ and $\bar{M}_{KP}$ from both MMS (left) and the simulation (right) in the same format as Figure 4. We note that s and s_M do not have real units on the right-axis because the units are not physical[22]. From 22:34:00-1.95 (the left-edge of the gold box), MMS3 made a brief excursion into the inflow region[39] where entropy reaches a maximum during the separatrix crossing and a minimum at the furthest excursion. During the same interval, the non-Maxwellianity peaks in the inflow region, a characteristic that has been noted in previous simulations of reconnection[31]. That non-Maxwellianity peaks outside of the regions where energy is being dissipated will be discussed below in the context of the electron distribution functions.

As MMS3 enters into the EDR (the gold box), passes southward of the X-line, and exits into the tailward exhaust, entropy density gradually increases in the observations; however, in the simulation, entropy density has a U-shaped profile with a minimum below the EDR. As expected from Eq. 9, these traces have the same overall structure as the density profiles in Figure 4a,i.

The non-Maxwellianity measure $\bar{M}_{KP}$ (Eq. 11, Fig. 5d,g) is computed using both s (Eq. 7, blue) and s_V (Eq. 15, green). The MMS observations result in unphysical values within the EDR of the electron Kaufmann and Paterson non-Maxwellianity $\bar{M}_{KP,s,e}$ based on s, where it becomes negative. The Maxwellian distribution should have the highest entropy of any distribution with the same number of particles and energy, so $\bar{M}_{KP,s,e}$ should be positive. The reason $\bar{M}_{KP,s,e}$ is negative will be explained in §V. In contrast, the electron Kaufmann and Paterson non-Maxwellianity $\bar{M}_{KP,s_V,e}$ using the velocity space entropy density s_V is always positive, consistent with theoretical constraints.

The other non-Maxwellianity measure $\bar{M}$ (Fig. 4d,g, orange) is computed using the appropriate version of Eq. 12 for MMS and the simulation. It is smaller in magnitude than $\bar{M}_{KP}$ because its normalization term s_V ensures that $\bar{M}$ is bounded to the range [0,1] for a properly defined velocity space grid[24]. When comparing observations to simulations, both $\bar{M}$ and $\bar{M}_{KP}$ have similar shapes within the EDR despite the fact that s and s_V are different. In addition, both values of $\bar{M}$ are more similar in magnitude than the values of $\bar{M}_{KP}$. This implies that the local measure of kinetic entropy density s_V as measured in the closed simulation can be interpreted in the same manner as it is in the large, open magnetotail system by MMS.

Now we relate kinetic entropy measurements to various kinetic processes that occur dur-
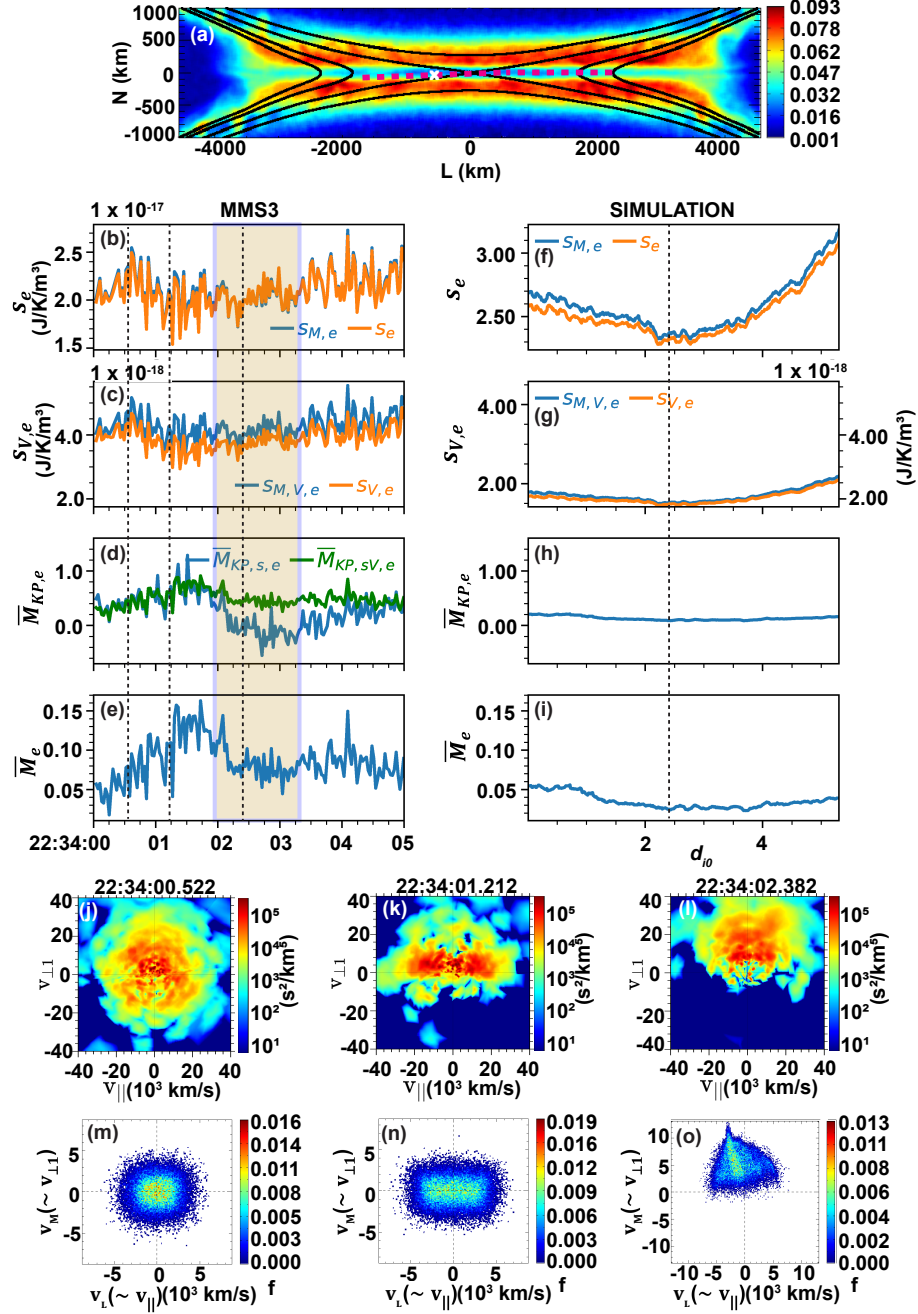
FIG. 5. Kinetic entropy and non-Maxwellianity in an EDR and their relationship to structures in the distribution function. (a) 2D plot of electron non-Maxwellianity $\bar{M}_e$ in the PIC simulation, the virtual satellite trajectory through the EDR, representative magnetic field lines, and the location of the EDR distribution in panel o, marked by an "x". (b,f) Total and (c,g) velocity space kinetic entropy density for the measured (orange) and Maxwellianized (blue) distributions. (d,h) Kaufmann and Paterson non-Maxwellianity $\bar{M}_{KP}$ using total (blue) and velocity space (green) entropy density. (e,i) Velocity space non-Maxwellianity $\bar{M}$ (orange). For (b)-(i), MMS data is in the left column and simulation data is in the right column. (j,m) Upstream, (k,n) inflow, and (l,o) EDR electron distribution functions from MMS3 (j-l) and the PIC simulation (m-o).

ing reconnection by examining the electron distribution functions in the MMS data (Fig. 5j-l) and the PIC simulation (Fig. 5m-o) at the times and locations indicated by vertical dashed lines in Figures 5b-i and by the "x" in the EDR of Figure 5a. The simulated distributions are on a different scale; as noted, multiplying the axes by $\sqrt{m_i/m_e} \approx 4.3$ will give the proper ranges for a real mass ratio simulation. The two simulated distributions corresponding to the MMS observations outside the EDR were taken from representative upstream locations in the simulation. The first distribution (Fig. 5j,m) is taken from the Earthward exhaust after the electrons have re-magnetized and become mostly Maxwellian. The second distribution (Fig. 5k,n) is from the inflow region where parallel potential structures generate a temperature anisotropy[63,64]. Here s_V is lower, but the non-Maxwellianity is relatively large. The third distribution (Fig. 5l,o) is from the heart of the EDR where meandering motion in the current sheet creates crescents and striations[34,36,39]. Here, the non-Maxwellianity is intermediate between the inflow and Maxwellian distributions. That regions of elevated non-Maxwellianity in the MMS observations can be related to kinetic processes during reconnection is consistent with previous numerical simulations[31] and motivates the utility of the entropy-based non-Maxwellianity measure as an indicator of kinetic-scale energy conversion and dissipation processes that occur during reconnection.

V.   INFORMATION LOSS

The differences in non-Maxwellianity measures demonstrated in Figure 5 come about because of subtle differences in the combinatorial and semi-continuous forms of entropy derived in § II. In the combinatorial form of entropy, we break up phase space into bins of size $\Delta^3 r \Delta^3 v$ and count the number of arrangements of particles within each bin. There is a direct relationship between the number of particles and the grid scale that becomes apparent when the bins become too small and Stirling's approximation is no longer valid. In the semi-continuous form of entropy, we coarse-grain phase space and represent the system of particles with a distribution function, tacitly assuming that our choice of grid sizes is appropriate and that the statistics in each cell are sufficient. In practice, however, there is no way to ensure this assumption holds for every distribution of particles that we encounter. As a result of the assumption, we lose the connection between the distribution function, the grid size, and the actual number of particles within each bin. Two important consequences are that 1) the

definition of total entropy density s defined in Eq. 7 lacks information connecting the grid scale $\Delta^3 v$ to the number density n of particles within each cell and 2) the total Maxwellian entropy density, s_M defined in Eq. 9, lacks information connecting the grid scale $\Delta^3 v$ to the thermal velocity of the distribution $v_{th} = \sqrt{2k_B T/m}$. This missing information results in unphysical values for $\bar{M}_{KP}$ in Figure 5d. The definition of s_V adds that information back in, as represented by the $n(\mathbf{r})/\Delta^3 v$ in the first term of Eq. 6, and by the $v_{th}^2/(\Delta^3 v)^{2/3}$ factor in the result for $s_{M,V}$ (Eq. 10). As a result, $\bar{M}_{KP,s_V}$ is positive definite. The dependence on $\Delta^3 v$ serves to regularize $\bar{M}_{KP}$ to give $\bar{M}$ and is present in the denominator of Eq. 13 that relates the two non-Maxwellianity measures[24]. We interpret the denominator as the amount of "information" lost when a grid scale is imposed on velocity space, and we investigate it further here.

As a demonstration of the effect of the course-grained, non-uniform velocity-space grid on the distribution function, we return to the discussion of why $\bar{M}_{KP,s,e} < 0$ within the EDR but $\bar{M}_{KP,s_V,e}$ is always positive (shown again in Fig 6f,g). Looking at the final term of s_V in Eq. 15, we see a correction due to the non-uniformity of the velocity-space grid. This means that, in the computation of s (Eq. 7), non-Maxwellian structures in the EDR are weighted more heavily by the non-uniform velocity space bins than the associated populations in the Maxwellianized distribution. By including the correction term, $\bar{M}_{KP,s_V,e} > 0$ throughout the interval, as it should be on theoretical grounds.

To quantify the information loss as a result of discretizing velocity space, we write the expressions for $\bar{M}$ for the MMS and simulation equations in the form

$$\bar{M} = R(\bar{M}_{KP} + B_{cg}), \tag{27}$$

where B_{cg} is a bias and R is a regularization factor that arise from course graining velocity space; in the simulations with a uniform velocity-space grid, $B_{cg} = 0$. Figure 6 shows the information loss for the MMS data (Eq. 17), which has non-uniform velocity-space bins. The first two MMS panels (a,b) show s and s_V for the measured and associated Maxwellian distributions for context. Panels (c-e) plot B_{cg}, R, and RB_{cg}, and panels (f-h) contain $\bar{M}_{KP}$ (Eq. 11) and $\bar{M}$ (Eqs. 16 and 17) to facilitate understanding where the information loss leads to issues in the calculated values of non-Maxwellianity.

The bias term B_{cg} significantly departs from 0 within the EDR; this is also where $\bar{M}_{KP} < 0$. For comparison, $\bar{M} > 0$ in the same region. The reason is that the correction for non-
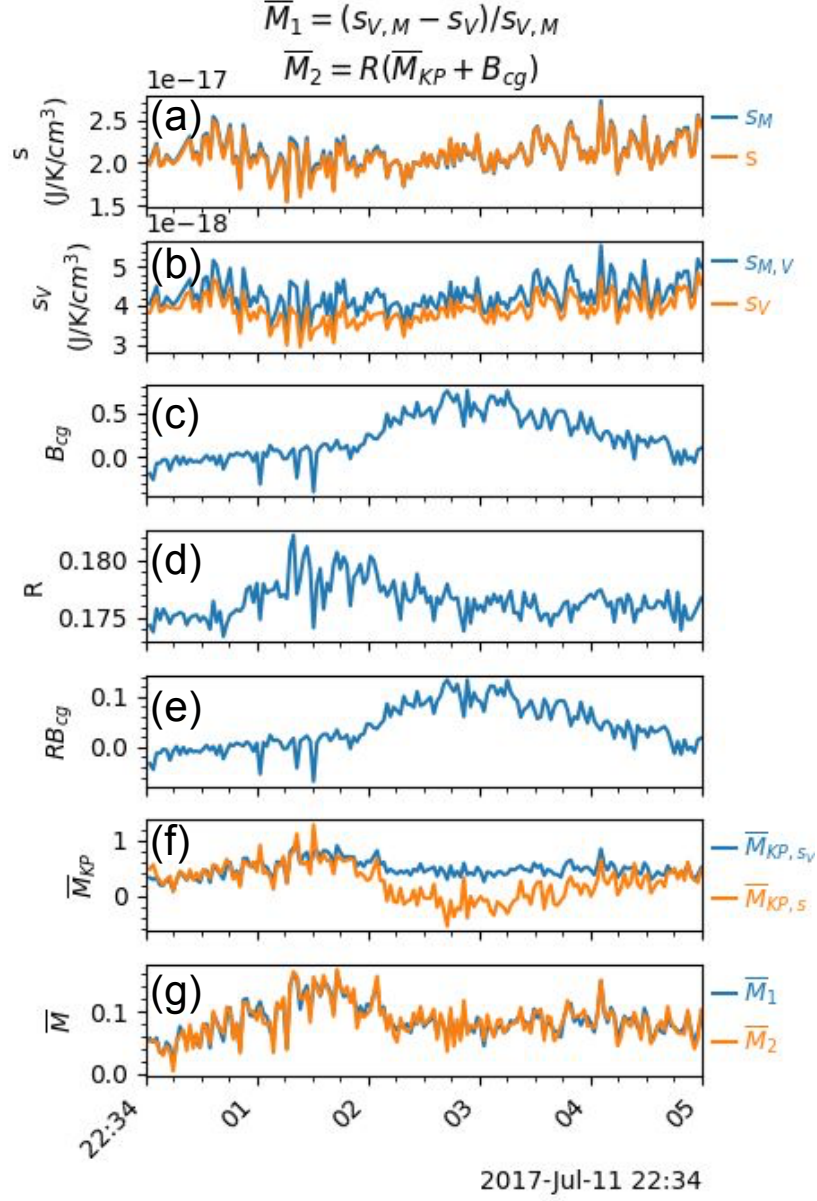
FIG. 6. Analysis of information loss as a result of coarse graining velocity space in the MMS observations. (a,b) Total s and velocity space s_V entropy densities in the same format as Figure 5b,c. (c) Bias B_{cg}, (d) regularization R, and (e) their product. non-Maxwellianity terms (f) $\bar{M}_{KP}$ calculated using s and s_V, and (g) $\bar{M}$ calculated from Equations 25 and 26.

uniform velocity-space grid in s_V propagates into B_{cg}. Given that

$$B_{cg} = -\frac{2}{3n} \int d^3 v(\mathbf{v}) \ln \left[d^3 v(\mathbf{v}) \right] \left[f_M(\mathbf{v}) - f(\mathbf{v}) \right], \tag{28}$$

and noting that the density of the observed and Maxwellianized distributions are the same,

it is the $\ln\left[d^3v(\mathbf{v})\right]$ factor that weighs the measured non-Maxwellian distribution structures present in the EDR more heavily than the associated populations in the Maxwellianized distribution. By correcting for the non-uniform velocity-space grid, B_{cg} makes $\bar{M} > 0$.

The regularization term R serves to scale $\bar{M}_{KP}$ into the range $[0,1]$ so that $\bar{M}$ is normalized for an appropriate velocity-space grid size[24] (Fig. 6g). From Equation 17, the regularization term R_{MMS} for MMS observations is

$$R_{MMS} = \left[1 + \ln\left(\frac{2\pi k_B T}{m}\right) - \frac{2}{3n}\int d^3v(\mathbf{v})\ln\left[d^3v(\mathbf{v})\right]f_M(\mathbf{v})\right]^{-1}, \qquad (29)$$

which contains the natural log of the thermal velocity $v_{th} = \sqrt{2k_B T/m}$ and the Maxwellianized distribution weighted by the natural log of the bin volume. When $d^3v(\mathbf{v})$ is uniform, we recover the regularization factor for a uniform velocity-space grid (Eq. 13, §II):

$$R_{Sim} = \left(1 + \ln\left[\pi v_{th}^2/(\Delta^3 v)^{2/3}\right]\right)^{-1}. \qquad (30)$$

The simulation regularization factor is plotted in Figure 7a as a function of distance along the virtual spacecraft trajectory. As seen in Figure 5g, $\bar{M}$ is normalized in the simulations such that its magnitude is similar to the observations.

Together, R and B_{cg} represent the amount of information lost by coarse-graining velocity space. B_{cg} depends only on the uniformity of the velocity-space grid, while R additionally depends on the relative size of the velocity-space grid scale and the thermal speed[22,24]. Consequently, it can be different for ions than for electrons. This has implications for satellite missions like MMS that study dissipation processes, as discussed further in the next section.

To better understand the dependence of information loss on velocity-space bin size and the plasma environment being sampled, Figure 7b shows contours of $R_{Sim}(\Delta v, v_{th})$ on a log-log scale. Information loss is minimized when $\bar{M}_{KP} = \bar{M}$, or when $R_{Sim} = 1$ (green line); it occurs where $\Delta v = \sqrt{\pi}v_{th}$ and will be discussed in greater detail in the sections that follow. When $\Delta v \ll \sqrt{\pi}v_{th}$, the distribution is over-resolved and there are too few particles per bin. When $\Delta v \gg \sqrt{\pi}v_{th}$, the distribution is under-resolved and important structures can be lost. In both of these limits, $R \to 0$ to compensate for $\bar{M}_{KP} \to \infty$[24]. Another critical point is $\Delta v = \sqrt{\pi e}v_{th}$. There, $R \to \pm\infty$ indicating that $\bar{M} \to \pm\infty$ while $\bar{M}_{KP}$ remains finite. This is because the choice of grid scale makes $s_{M,V} \to 0$ such that the observed distribution appears to be infinitely far from equilibrium.
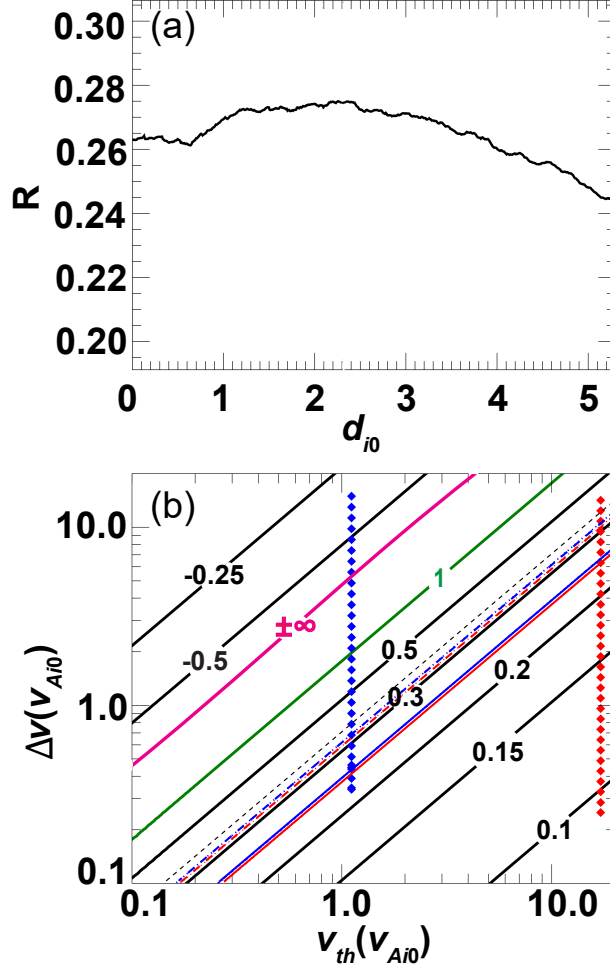
FIG. 7. (a) Variations in the regularization term variation as a function of distance along the virtual spacecraft trajectory. (b) Contours of the regularization term R as a function of thermal speed v_{th} and linear velocity space grid scale Δv. Black dashed lines show the optimized bin size from Liang et al.[22], dash-dotted and solid lines show the optimized bins with respect to the background and current sheet populations, respectively, for our simulation. Data for ions and electrons are shown in blue and red, respectively. Diamond data points show the logarithmically-spaced velocity space bins used in MMS instruments.

In the PIC simulation presented here, the way we choose our velocity space grid-scale is described in §III C. The black dashed line represents the approximate ideal velocity-space grid size from Liang et al.[22] The dashed lines are the optimal velocity-space ion (blue) and electron (red) grid sizes for the background (dotted) and current sheet (solid line) populations used in this study. The difference between these lines and the line $R_{Sim} = 1$ is

discussed below. Because the bin spacing is uniform, the grid scale falls on a line of constant R_{Sim}.

For comparison, the MMS ion (blue) and electron (red) velocity-space bin sizes are shown in diamonds for the average thermal velocity ($\langle v_{th,i} \rangle = 973 \, \text{km/s}$ and $\langle v_{th,e} \rangle = 14,997 \, \text{km/s}$ with $\langle T_i \rangle = 4943 \, \text{eV}$ and $\langle T_e \rangle = 638 \, \text{eV}$) within the EDR. Because of the non-uniform grid spacing, each bin suffers from a different amount of information loss. The ion bin sizes are somewhat evenly spaced around $R_{sim} = 1$ and overlap with the ideal simulation grid sizes. The smallest bins overlap with the optimal velocity-space grid size in the simulations but correspond to energy channels far below the bulk ion energy (Fig. 1b). Meanwhile, the majority of electron bins over-resolve the distribution and none reach the line of $R_{Sim} = 1$. The highest energy bins overlap with the optimized simulation bin sizes, but these correspond to the highest energy channels and extend beyond the upper edge of the energy distribution (Fig. 1b). This means that MMS measurements suffer from information loss for both ions and electrons due to its non-uniformly spaced velocity-space grid and because the velocity-space bins that overlap with the energy spectra of the plasma are either too large or too small, so that they under- or over-resolve the distribution function.

VI. DISCUSSION

Entropy in a closed, isolated system never decreases, so it can be thought of in terms of a system's approach to equilibrium via the possible dissipation of energy and the irreversibility of the processes acting within it. A simulation with periodic boundary conditions is a closed system, so this interpretation can be directly applied to the simulated process – magnetic reconnection in our case. However, natural systems are open. In Earth's magnetotail, at the smallest scales, the electron diffusion region receives energy from the upstream inflow region, and at the largest scale the magnetotail itself receives energy from the solar wind and ionosphere. In such cases, a measurement of entropy can no longer be interpreted in terms of the Second Law. This has led us to investigate local measures of entropy to determine if such quantities in closed systems can be used to help interpret measurements in open systems.

A local measure of entropy is also beneficial because spacecraft are unable to sample all of the accessible position space of a system, but particle detectors are designed to sample

all of velocity space. Instead of considering the macroscopic evolution of entropy as a system approaches equilibrium, we consider how close the local distribution of plasma is to equilibrium by comparing it to its Maxwellianized distribution. As we have seen, the parallel potential in the inflow region and the reconnection electric field in the EDR both do work to organize the distribution, reducing the number of available arrangements and producing low-entropy, high non-Maxwellianity states (see also Liang *et al.*[24]). non-Maxwellianity indicates the degree to which a distribution is organized and, therefore, can be used to identify regions where dissipation processes take place, like the EDR. Recent work has shown a connection between structures in the distribution and the Vlasov equation[65] and could lead to deeper insights into non-Maxwellianity.

Information loss arises from discretizing velocity space and can be enhanced when the bin size is not uniform. The non-uniform velocity-space grid used by FPI weights accelerated, non-gyrotropic structures in the distribution function more heavily than their associated Maxwellianized populations. As a result, a bias correction term appears in $\bar{M}$. This bias is not present when velocity bins are uniformly spaced. Additional information loss occurs if the velocity-space bin size is not chosen properly with respect to the thermal velocity of the plasma. This loss is enhanced with non-uniformly spaced bins and is different for ions and electrons. For ion and electron distributions of the same shape to have the same value of velocity space kinetic entropy, $s_{V,e} = s_{V,i}$, requires $v_{th,e}/\Delta v_e = v_{th,i}/\Delta v_i$. A result of information loss is that dissipation processes cannot be accurately measured[22], and the reversibility of dissipation processes cannot be determined. With regard to MMS, an analysis of the generalized Ohm's law during magnetopause reconnection revealed an unmeasured, residual amount of dissipated energy that was unaccounted for[32]. Preliminary analysis shows an intriguing similarity between information loss and this residue term.

Information loss is minimized if $\bar{M}_{KP} = \bar{M}$. This occurs most simply when the velocity space grid is uniform, making $B_{cs} = 0$ and reducing the regularization term R_{MMS} (Eq. 29) to R_{Sim} (Eq. 30); and when the R_{Sim} is unity, i.e., when $\Delta v = \sqrt{\pi} v_{th} \approx 1.77 v_{th}$. This suggests that the ideal bin size is slightly larger than the thermal velocity; however, simulations found best agreement with theoretical values when the bin size was $\Delta v \simeq 0.69 v_{th}$[22]. The discrepancy here is likely related to particle noise in PIC simulations, as higher numbers of particles per grid (> 100) would lead to better statistics at high speeds.

The contour where $\Delta v = \sqrt{\pi} v_{th}$ is associated with interesting characteristics of s_V and

$s_{M,V}$. If Δv is proportional to $\sqrt{T}$, as it is when $\Delta v = \sqrt{\pi} v_{th}$, then the Maxwellian velocity-space entropy density, $s_{M,V}$ in Eq. 10, is independent of temperature. If $\Delta v = \sqrt{\pi} v_{th}$ exactly, then $s_{M,V} = \frac{3}{2} k_B n = c_V n$, meaning $s_{M,V}$ is proportional to the amount of energy required to raise the temperature of an ideal gas in thermal equilibrium by one degree. Because there is no free energy in either the initial or final equilibrium states, the external work used to increase the temperature contributes directly to increasing the entropy. For this particularly chosen grid scale, we see that $\bar{M}_{KP} = (s_M - s)/s_{M,V}$, which is similar in form to $\bar{M}$ (Eq. 12) and implies that $s_M - s = s_{M,V} - s_V$. Finally, $\Delta v = \sqrt{\pi} v_{th}$ is the point where the logarithm in R_{Sim} transitions from positive to negative, which is a more intuitive point for indicating that the distribution is over- or under-resolved.

Considerations for minimizing information loss have clear implications for the design of particle instruments. In a simplified model, an electrostatic analyzer can be thought of as a curved parallel plate capacitor. The voltage on each plate selects the range and center energies E_k of the energy bins while the curvature of and separation between the plates determines the range of energies ΔE_k of the particles that can pass through the capacitor. For a given configuration, $\Delta E_k/E_k$ is constant, meaning ΔE_k increases with energy. An aperture can then be placed on the capacitor to limit the overall amount of flux into the device, thereby determining the instrument's geometric factor. A lot of care goes into deciding the requirements on E_k, ΔE_k, and the geometric factor, but ultimately the choice imposes a grid scale and count rate on the measured particle distribution. This means that information loss is inherent to all measurements and that new design considerations need to be taken into account to minimize it. The way to minimize it is to ensure that the velocity space bin sizes, $\Delta v_k = \Delta E_k/\sqrt{2mE_k}$, does not greatly over- or under-resolve the thermal velocity in the range of energies present in the energy distribution.

Other measures of non-Maxwellianity, including enstrophy[15], the Greco ϵ parameter[14], and the Graham ϵ parameter[26]

$$
\begin{aligned}
\Omega &= \int d^3v \, (f - f_M)^2 \\
\epsilon_{Greco} &= \frac{1}{n}\sqrt{\int d^3v \, (f - f_M)^2} \\
\epsilon_{Graham} &= \frac{1}{2n} \int d^3v \, |f - f_{biM}|,
\end{aligned}
$$

are not entropy-based and may not suffer as heavily from information loss as MKP. One reason is that the $\ln[f(\mathbf{v})]$ term in s enhances subtle variation in the distribution, similar to how

the powers of $\mathbf{v}$ affect higher-order moments. Unfortunately, these other non-Maxwellian parameters are all defined to be positive, meaning that unphysical negative values, like those shown in Figure 5 for $\bar{M}_{KP}$, are masked. While the Ω and ϵ non-Maxwellianity parameters are not entropy-based, there are approaches to calculating kinetic entropy in simulations beyond what were described in this paper (Jara-Almonte and Ji[27], and references therein). More work is needed to quantify non-Maxwellianity and information loss using those approaches.

While reconnection transfers energy from the fields to the plasma, it is not clear if there is an exchange of entropy between the particles and the electromagnetic fields. The fact that the reversibility of reconnection depends on the strength of the guide field[28,29] suggests that changes in entropy are due solely to plasma dynamics. In a closed, collisionless system (such as the simulation performed in this study) entropy is a conserved quantity; however, simulations have shown that both total energy and kinetic entropy are conserved to within numerical precision[22], meaning that while electromagnetic energy is converted entirely into particle kinetic energy, there is no similar exchange in entropy between the fields and the plasma. Interestingly, as we showed in Figure 5, plasma entropy is a local minimum in the EDR where structured distributions are found and electromagnetic energy is being dissipated. This suggests that the electromagnetic fields do work to organize the inflowing distribution (lowering the entropy) and that downstream processes thermalize it (increasing entropy). But are the electromagnetic fields simply a reservoir of energy or do they also exchange entropy? If plasma entropy is related to order and disorder, then similar considerations for the fields might suggest that waves and turbulence increase electromagnetic entropy. There exists a statistical description of radiation entropy that develops a quantity similar to $\bar{M}$ as the deviation of the observed radiation from an ideal black body[66], a Boltzmann H-theorem for classical wave modes that can be applied to waves often present during reconnection[67], and a formulation of the Second Law to describe an ensemble of turbulent eddies[68]. More work is needed to determine how such theories influence the evolution of kinetic entropy. This is relevant to both laboratory experiments like PHASMA[69] which directly measure distribution functions non-perturbatively and future space missions like HelioSwarm[70] that study turbulent processes leading to dissipation.

VII. SUMMARY

In this study, we examine kinetic entropy associated with dissipation processes occurring within a magnetotail electron diffusion region using both in-situ observations and a PIC simulation. We generalize the theory of kinetic entropy[22,42] to the case of non-uniform velocity space bins and transform them to spherical energy coordinates for application to experimental datasets. In doing so, we implement a Maxwellian look-up table to reduce numerical errors between the observed distribution and its associated Maxweillian. The theory is then applied to MMS observations of a magnetotail EDR and compared to the kinetic entropy density and non-Maxwellianity from a PIC simulation of the observed event. Good agreement between observations and simulations indicates that the insights gained from local kinetic entropy density and non-Maxwellianity measures in numerical simulations in a closed domain can be useful when interpreting observations in a naturally occurring open system.

We demonstrate that kinetic entropy density s leads to a non-Maxwellianity measure $\bar{M}_{KP}$ that is not positive definite, as it should be on physical grounds, because it is biased by the non-uniform velocity-space grid of MMS that weighs non-Maxwellian structures more heavily than their associated Maxwellianized structures. A similar issue is likely to be happening in previous observational studies using the quadratic non-Maxwellianity ϵ measure[14,15,26,71]. The velocity-space kinetic entropy s_V corrects for the non-uniform grid and results in a non-Maxwellianity measure $\bar{M}_{KP,s_V}$ that is positive definite, as it should be on theoretical grounds. We quantify the reason that s leads to unphysical results while s_V does not by introducing "information loss"; s lacks information connecting the grid scale to the number of particles within each cell. This information is contained in s_V and serves to regularize $\bar{M}_{KP}$ so that the resulting $\bar{M}$ is bounded. We show that $\bar{M}$ is capable of identifying non-Maxwellian distributions indicative of kinetic effects and dissipation processes that occur during reconnection.

The new concept of "information loss" is captured by two quantities, R and B_{cg}, that measure the extent to which the choice of velocity space grids affects measurements of kinetic entropy. We show that to minimize information loss, the velocity space grid scale needs to be chosen so that the thermal velocity of the plasma is not over- or under-resolved. This involves having a uniform velocity space grid with $\Delta v \approx \sqrt{\pi} v_{th}$. Unfortunately for

experimental particle detectors, a uniform velocity space grid is not possible; however, the energy resolution of the instrument $\Delta E_k / E_k$ can be optimized to minimize information loss by having $\Delta v_k = \Delta E_k / \sqrt{2mE_k}$ adequately resolve v_{th} within the energy range of the energy distribution. Thus, entropy and information loss are important considerations for satellite instrument development.

VIII.   SUPPLEMENTARY MATERIAL

The Supplementary Material contains more complete derivations of the kinetic entropy and other parameters derived and discussed in this work. This includes the alternate derivation of Eq. 2 described in §II A, the velocity-space kinetic entropy density, s_V, for both uniformly and non-uniformly spaced velocity-space grids (Eqs. 6 and 15), the condition for equal entropy for ions and electrons discussed in §VI, an alternate derivation of the relationship between $\bar{M}$ and $\bar{M}_{KP}$ (Eq. 13), and $\bar{M}$ for the case of non-uniform velocity space bins. It also contains transformations from (v_x, v_y, v_z) to (ϕ, θ, v), (ϕ, θ, E), and (ϕ, θ, U) for f_M, s, s_V, $\bar{M}$, as well as the density, velocity, and temperature moments of the distribution. Finally, it contains tables of the calculated moments and entropy parameters for a model, measured, and Maxwellianized distribution to serve as an demonstration of the numerical errors described in §IV A.

ACKNOWLEDGMENTS

IX.   DATA AVAILABILITY

MMS data is publicly available at the MMS science data center (https://lasp.colorado.edu/mms/sdc/public/)[72]. MMS data was processed and visualized with the help of the PyMMS Python library[73,74] Simulation data used in this manuscript is available on Zenodo (https://doi.org/10.5281/zenodo.5807744)[75].

REFERENCES

[1] G. G. Howes, "A prospectus on kinetic heliophysics," Physics of Plasmas **24**, 055907 (2017), _eprint: https://doi.org/10.1063/1.4983993.

[2] B. Lembege, J. Giacalone, M. Scholer, T. Hada, M. Hoshino, V. Krasnoselskikh, H. Kucharek, P. Savoini, and T. Terasawa, "Selected problems in collisionless-shock physics," Space Science Reviews **110**, 161–226 (2004).

[3] W. H. Matthaeus, "Turbulence in space plasmas: Who needs it?" Physics of Plasmas **28**, 032306 (2021), https://doi.org/10.1063/5.0041540.

[4] M. Hesse and P. A. Cassak, "Magnetic reconnection in the space sciences: Past, present, and future," Journal of Geophysical Research: Space Physics **125**, e2018JA025935 (2020), e2018JA025935 2018JA025935, https://agupubs.onlinelibrary.wiley.com/doi/pdf/10.1029/2018JA025935.

[5] E. G. Zweibel and M. Yamada, "Magnetic reconnection in astrophysical and laboratory plasmas," Annual Review of Astronomy and Astrophysics **47**, 291–332 (2009), https://doi.org/10.1146/annurev-astro-082708-101726.

[6] V. Angelopoulos, A. Runov, X.-Z. Zhou, D. L. Turner, S. A. Kiehas, S.-S. Li, and I. Shinohara, "Electromagnetic Energy Conversion at Reconnection Fronts," Science **341**, 1478–1482 (2013), publisher: American Association for the Advancement of Science _eprint: https://science.sciencemag.org/content/341/6153/1478.full.pdf.

[7] https://www.eia.gov/state/print.php?sid=NY.

[8] J. L. Burch and J. F. Drake, "Reconnecting Magnetic Fields: The huge amounts of energy released from the relinking of magnetic fields in outer space are both mysterious and potentially destructive," American Scientist **97**, 392–399 (2009), publisher: Sigma Xi, The Scientific Research Society URL: https://www.americanscientist.org/article/reconnecting-

magnetic-fields.

[9] A. Greco, P. Chuychai, W. H. Matthaeus, S. Servidio, and P. Dmitruk, "Intermittent MHD structures and classical discontinuities," Geophysical Research Letters **35** (2008), https://doi.org/10.1029/2008GL035454, _eprint: https://agupubs.onlinelibrary.wiley.com/doi/pdf/10.1029/2008GL035454.

[10] J. D. Scudder, R. D. Holdaway, R. Glassberg, and S. L. Rodriguez, "Electron diffusion region and thermal demagnetization," Journal of Geophysical Research **113**, 1–14 (2008).

[11] S. Zenitani, M. Hesse, A. Klimas, C. Black, and M. Kuznetsova, "The inner structure of collisionless magnetic reconnection: The electron-frame dissipation measure and Hall fields," Physics of Plasmas **18**, 122108 (2011).

[12] N. Aunai, M. Hesse, and M. Kuznetsova, "Electron nongyrotropy in the context of collisionless magnetic reconnection," Physics of Plasmas (1994-present) **20**, 1–6 (2013).

[13] M. Swisdak, "Quantifying gyrotropy in magnetic reconnection," Geophysical Research Letters **43**, 43–49 (2016).

[14] A. Greco, F. Valentini, S. Servidio, and W. H. Matthaeus, "Inhomogeneous kinetic effects related to intermittent magnetic discontinuities," Phys. Rev. E **86**, 66405 (2012), publisher: American Physical Society.

[15] S. Servidio, A. Chasapis, W. H. Matthaeus, D. Perrone, F. Valentini, T. N. Parashar, P. Veltri, D. Gershman, C. T. Russell, B. Giles, S. A. Fuselier, T. D. Phan, and J. Burch, "Magnetospheric Multiscale Observation of Plasma Velocity-Space Cascade: Hermite Representation and Theory," Phys. Rev. Lett. **119**, 205101 (2017), publisher: American Physical Society.

[16] J. L. Burch, T. E. Moore, R. B. Torbert, and B. L. Giles, "Magnetospheric Multiscale Overview and Science Objectives," Space Science Reviews **199**, 5–21 (2015), publisher: Springer Netherlands.

[17] L.-J. Chen, N. Bessho, B. Lefebvre, H. Vaith, A. Asnes, O. Santolik, A. Fazakerley, P. Puhl-Quinn, A. Bhattacharjee, Y. Khotyaintsev, P. Daly, and R. Torbert, "Multispacecraft observations of the electron current sheet, neighboring magnetic islands, and electron acceleration during magnetotail reconnection," Physics of Plasmas **16**, 056501 (2009).

[18] M. Hesse, N. Aunai, D. Sibeck, and J. Birn, "On the electron diffusion region in planar, asymmetric, systems," Geophysical Research Letters **41**, 8673–8680 (2014), https://agupubs.onlinelibrary.wiley.com/doi/pdf/10.1002/2014GL061586.

[19] J. L. Burch, R. B. Torbert, T. D. Phan, L.-J. Chen, T. E. Moore, R. E. Ergun, J. P. Eastwood, D. J. Gershman, P. A. Cassak, M. R. Argall, S. Wang, M. Hesse, C. J. Pollock, B. L. Giles, R. Nakamura, B. H. Mauk, S. A. Fuselier, C. T. Russell, R. J. Strangeway, J. F. Drake, M. A. Shay, Y. V. Khotyaintsev, P.-A. Lindqvist, G. Marklund, F. D. Wilder, D. T. Young, K. Torkar, J. Goldstein, J. C. Dorelli, L. A. Avanov, M. Oka, D. N. Baker, A. N. Jaynes, K. A. Goodrich, I. J. Cohen, D. L. Turner, J. F. Fennell, J. B. Blake, J. Clemmons, M. Goldman, D. Newman, S. M. Petrinec, K. J. Trattner, B. Lavraud, P. H. Reiff, W. Baumjohann, W. Magnes, M. Steller, W. Lewis, Y. Saito, V. Coffey, and M. Chandler, "Electron-scale measurements of magnetic reconnection in space," Science **352** (2016), 10.1126/science.aaf2939, publisher: American Association for the Advancement of Science ISBN: 1223326500.

[20] J. M. Webster, J. L. Burch, P. H. Reiff, A. G. Daou, K. J. Genestreti, D. B. Graham, R. B. Torbert, R. E. Ergun, S. Y. Sazykin, A. Marshall, R. C. Allen, L. J. Chen, S. Wang, T. D. Phan, B. L. Giles, T. E. Moore, S. A. Fuselier, G. Cozzani, C. T. Russell, S. Eriksson, A. C. Rager, J. M. Broll, K. Goodrich, and F. Wilder, "Magnetospheric Multiscale Dayside Reconnection Electron Diffusion Region Events," Journal of Geophysical Research: Space Physics **123**, 4858–4878 (2018).

[21] N. Bessho, L.-J. Chen, and M. Hesse, "Electron distribution functions in the diffusion region of asymmetric magnetic reconnection," Geophysical Research Letters **43**, 1828–1836 (2016).

[22] H. Liang, P. A. Cassak, S. Servidio, M. A. Shay, J. F. Drake, M. Swisdak, M. R. Argall, J. C. Dorelli, E. E. Scime, W. H. Matthaeus, V. Roytershteyn, and G. L. Delzanno, "Decomposition of plasma kinetic entropy into position and velocity space and the use of kinetic entropy in particle-in-cell simulations," Physics of Plasmas **26**, 82903 (2019).

[23] R. L. Kaufmann and W. R. Paterson, "Boltzmann H function and entropy in the plasma sheet," Journal of Geophysical Research: Space Physics **114**, A00D04 (2009).

[24] H. Liang, M. H. Barbhuiya, P. A. Cassak, O. Pezzi, S. Servidio, F. Valentini, and G. P. Zank, "Kinetic entropy-based measures of distribution function non-Maxwellianity: theory and simulations," Journal of Plasma Physics **86**, 825860502 (2020), publisher: Cambridge University Press.

[25] G. K. Parks, E. Lee, M. McCarthy, M. Goldstein, S. Y. Fu, J. B. Cao, P. Canu, N. Lin, M. Wilber, I. Dandouras, H. Réme, and A. Fazakerley, "Entropy Generation across Earth's

Collisionless Bow Shock," Phys. Rev. Lett. **108**, 061102 (2012), publisher: American Physical Society.

[26] D. B. Graham, Y. V. Khotyaintsev, M. André, A. Vaivads, A. Chasapis, W. H. Matthaeus, A. Retino, F. Valentini, and D. J. Gershman, "Non-Maxwellianity of electron distributions near Earth's magnetopause," (2021), _eprint: 2102.09639.

[27] J. Jara-Almonte and H. Ji, "Thermodynamic Phase Transition in Magnetic Reconnection," Phys. Rev. Lett. **127**, 055102 (2021), publisher: American Physical Society.

[28] A. Ishizawa and T.-H. Watanabe, "Reversible collisionless magnetic reconnection," Physics of Plasmas **20**, 102116 (2013), _eprint: https://doi.org/10.1063/1.4826201.

[29] M. Xuan, M. Swisdak, and J. F. Drake, "The Reversibility Of Magnetic Reconnection," Phys. Plasmas **28**, 092107 (2021).

[30] R. Numata and N. F. Loureiro, "Ion and electron heating during magnetic reconnection in weakly collisional plasmas," Journal of Plasma Physics **81**, 305810201 (2015), publisher: Cambridge University Press.

[31] H. Liang, P. A. Cassak, M. Swisdak, and S. Servidio, "Estimating Effective Collision Frequency and Kinetic Entropy Uncertainty in Particle-in-Cell Simulations," Journal of Physics: Conference Series **1620**, 012009 (2020), publisher: IOP Publishing.

[32] R. B. Torbert, J. L. Burch, B. L. Giles, D. Gershman, C. J. Pollock, J. Dorelli, L. Avanov, M. R. Argall, J. Shuster, R. J. Strangeway, C. T. Russell, R. E. Ergun, F. D. Wilder, K. Goodrich, H. A. Faith, C. J. Farrugia, P.-A. Lindqvist, T. Phan, Y. Khotyaintsev, T. E. Moore, G. Marklund, W. Daughton, W. Magnes, C. A. Kletzing, and S. Bounds, "Estimates of terms in Ohm's law during an encounter with an electron diffusion region," Geophysical Research Letters **43**, 5918–5925 (2016).

[33] A. S. Afshari, G. G. Howes, C. A. Kletzing, D. P. Hartley, and S. A. Boardsen, "Electron Landau Damping of Turbulence in the Terrestrial Magnetosheath Plasma," Earth and Space Science Open Archive , 20 (2020).

[34] J. Ng, J. Egedal, A. Le, W. Daughton, and L.-J. Chen, "Kinetic Structure of the Electron Diffusion Region in Antiparallel Magnetic Reconnection," Phys. Rev. Lett. **106**, 65002 (2011), publisher: American Physical Society.

[35] J. R. Shuster, L.-J. Chen, W. S. Daughton, L. C. Lee, K. H. Lee, N. Bessho, R. B. Torbert, G. Li, and M. R. Argall, "Highly structured electron anisotropy in collisionless reconnection exhausts," Geophysical Research Letters **41**, 5389–5395 (2014).

[36] J. R. Shuster, L.-J. Chen, M. Hesse, M. R. Argall, W. Daughton, R. B. Torbert, and N. Bessho, "Spatiotemporal evolution of electron characteristics in the electron diffusion region of magnetic reconnection: Implications for acceleration and heating," Geophysical Research Letters **42**, 2586–2593 (2015).

[37] M. Hoshino, T. Mukai, T. Terasawa, and I. Shinohara, "Suprathermal electron acceleration in magnetic reconnection," Journal of Geophysical Research: Space Physics **106**, 25979–25997 (2001).

[38] J. Egedal, A. Le, W. Daughton, B. Wetherton, P. A. Cassak, L.-J. Chen, B. Lavraud, R. B. Torbert, J. Dorelli, D. J. Gershman, and L. A. Avanov, "Spacecraft Observations and Analytic Theory of Crescent-Shaped Electron Distributions in Asymmetric Magnetic Reconnection," Phys. Rev. Lett. **117**, 185101 (2016), publisher: American Physical Society.

[39] R. B. Torbert, J. L. Burch, T. D. Phan, M. Hesse, M. R. Argall, J. Shuster, R. E. Ergun, L. Alm, R. Nakamura, K. J. Genestreti, D. J. Gershman, W. R. Paterson, D. L. Turner, I. Cohen, B. L. Giles, C. J. Pollock, S. Wang, L.-J. Chen, J. E. Stawarz, J. P. Eastwood, K. J. Hwang, C. Farrugia, I. Dors, H. Vaith, C. Mouikis, A. Ardakani, B. H. Mauk, S. A. Fuselier, C. T. Russell, R. J. Strangeway, T. E. Moore, J. F. Drake, M. A. Shay, Y. V. Khotyaintsev, P.-A. Lindqvist, W. Baumjohann, F. D. Wilder, N. Ahmadi, J. C. Dorelli, L. A. Avanov, M. Oka, D. N. Baker, J. F. Fennell, J. B. Blake, A. N. Jaynes, O. Le Contel, S. M. Petrinec, B. Lavraud, and Y. Saito, "Electron-scale dynamics of the diffusion region during symmetric magnetic reconnection in space," Science **362**, 1391–1395 (2018), publisher: American Association for the Advancement of Science.

[40] M. R. Argall, K. Paulson, L. Alm, A. Rager, J. Dorelli, J. Shuster, S. Wang, R. B. Torbert, H. Vaith, I. Dors, M. Chutter, C. Farrugia, J. Burch, C. Pollock, B. Giles, D. Gershman, B. Lavraud, C. T. Russell, R. Strangeway, W. Magnes, P.-A. Lindqvist, Y. V. Khotyaintsev, R. E. Ergun, and N. Ahmadi, "Electron Dynamics Within the Electron Diffusion Region of Asymmetric Reconnection," Journal of Geophysical Research: Space Physics **123**, 146–162 (2018).

[41] D. S. Payne, K. J. Genestreti, K. Germaschewski, M. R. Argall, R. B. Torbert, I. Dors, and A. Ardakani, "Energy Balance and Time Dependence of a Magnetotail Electron Diffusion Region," Journal of Geophysical Research: Space Physics **125**, e2020JA028290 (2020).

[42]L. Boltzmann, "Über die beziehung dem zweiten haubtsatze der mechanischen wärmetheorie und der wahrscheinlichkeitsrechnung resp. dem sätzen über das wäarmegleichgewicht," Wiener Berichte **76**, 373–435 (1877), in (Boltzmann 1909) Vol. II, paper 42.

[43]C. Mouhot and C. Villani, "On Landau damping," Acta Mathematica **207**, 29 – 201 (2011).

[44]C. Pollock, T. Moore, A. Jacques, J. Burch, U. Gliese, Y. Saito, T. Omoto, L. Avanov, A. Barrie, V. Coffey, J. Dorelli, D. Gershman, B. Giles, T. Rosnack, C. Salo, S. Yokota, M. Adrian, C. Aoustin, C. Auletti, S. Aung, V. Bigio, N. Cao, M. Chandler, D. Chornay, K. Christian, G. Clark, G. Collinson, T. Corris, A. De Los Santos, R. Devlin, T. Diaz, T. Dickerson, C. Dickson, A. Diekmann, F. Diggs, C. Duncan, A. Figueroa-Vinas, C. Firman, M. Freeman, N. Galassi, K. Garcia, G. Goodhart, D. Guererro, J. Hageman, J. Hanley, E. Hemminger, M. Holland, M. Hutchins, T. James, W. Jones, S. Kreisler, J. Kujawski, V. Lavu, J. Lobell, E. LeCompte, A. Lukemire, E. MacDonald, A. Mariano, T. Mukai, K. Narayanan, Q. Nguyan, M. Onizuka, W. Paterson, S. Persyn, B. Piepgrass, F. Cheney, A. Rager, T. Raghuram, A. Ramil, L. Reichenthal, H. Rodriguez, J. Rouzaud, A. Rucker, M. Samara, J.-A. Sauvaud, D. Schuster, M. Shappirio, K. Shelton, D. Sher, D. Smith, K. Smith, S. Smith, D. Steinfeld, R. Szymkiewicz, K. Tanimoto, J. Taylor, C. Tucker, K. Tull, A. Uhl, J. Vloet, P. Walpole, S. Weidner, D. White, G. Winkert, P.-S. Yeh, and M. Zeuch, "Fast Plasma Investigation for Magnetospheric Multiscale," Space Science Reviews **199**, 331–406 (2016).

[45]D. Moseev and M. Salewski, "Bi-Maxwellian, slowing-down, and ring velocity distributions of fast ions in magnetized plasmas," Physics of Plasmas **26**, 20901 (2019).

[46]https://lasp.colorado.edu/mms/sdc/public/.

[47]R. B. Torbert, C. T. Russell, W. Magnes, R. E. Ergun, P.-A. Lindqvist, O. Le Contel, H. Vaith, J. Macri, S. Myers, D. Rau, J. Needell, B. King, M. Granoff, M. Chutter, I. Dors, G. Olsson, Y. V. Khotyaintsev, A. Eriksson, C. A. Kletzing, S. Bounds, B. Anderson, W. Baumjohann, M. Steller, K. Bromund, G. Le, R. Nakamura, R. J. Strangeway, H. K. Leinweber, S. Tucker, J. Westfall, D. Fischer, F. Plaschke, J. Porter, and K. Lappalainen, "The FIELDS Instrument Suite on MMS: Scientific Objectives, Measurements, and Data Products," Space Science Reviews **199**, 105–135 (2016), publisher: Springer Netherlands.

[48]C. T. Russell, B. J. Anderson, W. Baumjohann, K. R. Bromund, D. Dearborn, D. Fischer, G. Le, H. K. Leinweber, D. Leneman, W. Magnes, J. D. Means, M. B. Moldwin,

R. Nakamura, D. Pierce, F. Plaschke, K. M. Rowe, J. A. Slavin, R. J. Strangeway, R. Torbert, C. Hagen, I. Jernej, A. Valavanoglou, and I. Richter, "The Magnetospheric Multiscale Magnetometers," Space Science Reviews **199**, 189–256 (2014), publisher: Springer Netherlands.

[49] P.-A. Lindqvist, G. Olsson, R. B. Torbert, B. King, M. Granoff, D. Rau, G. Needell, S. Turco, I. Dors, P. Beckman, J. Macri, C. Frost, J. Salwen, A. Eriksson, L. Åhlén, Y. V. Khotyaintsev, J. Porter, K. Lappalainen, R. E. Ergun, W. Wermeer, and S. Tucker, "The Spin-Plane Double Probe Electric Field Instrument for MMS," Space Science Reviews **199**, 137–165 (2014), publisher: Springer Netherlands.

[50] R. E. Ergun, S. Tucker, J. Westfall, K. A. Goodrich, D. M. Malaspina, D. Summers, J. Wallace, M. Karlsson, J. Mack, N. Brennan, B. Pyke, P. Withnell, R. Torbert, J. Macri, D. Rau, I. Dors, J. Needell, P.-A. Lindqvist, G. Olsson, and C. M. Cully, "The Axial Double Probe and Fields Signal Processing for the MMS Mission," Space Science Reviews **199**, 167–188 (2014), publisher: Springer Netherlands.

[51] R. Nakamura, K. J. Genestreti, T. Nakamura, W. Baumjohann, A. Varsani, T. Nagai, N. Bessho, J. L. Burch, R. E. Denton, J. P. Eastwood, R. E. Ergun, D. J. Gershman, B. L. Giles, H. Hasegawa, M. Hesse, P.-A. Lindqvist, C. T. Russell, J. E. Stawarz, R. J. Strangeway, and R. B. Torbert, "Structure of the Current Sheet in the 11 July 2017 Electron Diffusion Region Event," Journal of Geophysical Research: Space Physics **124**, 1173–1186 (2019), _eprint: https://agupubs.onlinelibrary.wiley.com/doi/pdf/10.1029/2018JA026028.

[52] K. J. Genestreti, T. K. M. Nakamura, R. Nakamura, R. E. Denton, R. B. Torbert, J. L. Burch, F. Plaschke, S. A. Fuselier, R. E. Ergun, B. L. Giles, and C. T. Russell, "How Accurately Can We Measure the Reconnection Rate EM for the MMS Diffusion Region Event of 11 July 2017?" Journal of Geophysical Research: Space Physics **123**, 9130–9149 (2018), _eprint: https://agupubs.onlinelibrary.wiley.com/doi/pdf/10.1029/2018JA025711.

[53] J. E. Stawarz, J. P. Eastwood, K. J. Genestreti, R. Nakamura, R. E. Ergun, D. Burgess, J. L. Burch, S. A. Fuselier, D. J. Gershman, B. L. Giles, O. Le Contel, P.-A. Lindqvist, C. T. Russell, and R. B. Torbert, "Intense Electric Fields and Electron-Scale Substructure Within Magnetotail Flux Ropes as Revealed by the Magnetospheric Multiscale Mission," Geophysical Research Letters **45**, 8783–8792 (2018).

[54] W.-L. Teh, T. Nakamura, R. Nakamura, and T. Umeda, "Oblique Ion-Scale Magnetotail Flux Ropes Generated by Secondary Tearing Modes," Jour-

nal of Geophysical Research: Space Physics **123**, 8122–8130 (2018), _eprint: https://agupubs.onlinelibrary.wiley.com/doi/pdf/10.1029/2018JA025775.

[55] T. K. M. Nakamura, K. J. Genestreti, Y.-H. Liu, R. Nakamura, W.-L. Teh, H. Hasegawa, W. Daughton, M. Hesse, R. B. Torbert, J. L. Burch, and B. L. Giles, "Measurement of the Magnetic Reconnection Rate in the Earth's Magnetotail," Journal of Geophysical Research: Space Physics **123**, 9150–9168 (2018).

[56] H. Hasegawa, R. E. Denton, R. Nakamura, K. J. Genestreti, T. K. M. Nakamura, K.-J. Hwang, T. D. Phan, R. B. Torbert, J. L. Burch, B. L. Giles, D. J. Gershman, C. T. Russell, R. J. Strangeway, P.-A. Lindqvist, Y. V. Khotyaintsev, R. E. Ergun, N. Kitamura, and Y. Saito, "Reconstruction of the Electron Diffusion Region of Magnetotail Reconnection Seen by the MMS Spacecraft on 11 July 2017," Journal of Geophysical Research: Space Physics **124**, 122–138 (2019), _eprint: https://agupubs.onlinelibrary.wiley.com/doi/pdf/10.1029/2018JA026051.

[57] J. Egedal, J. Ng, A. Le, W. Daughton, B. Wetherton, J. Dorelli, D. Gershman, and A. Rager, "Pressure tensor elements breaking the frozen-in law during reconnection in earth's magnetotail," Physical Review Letters **123** (2019), 10.1103/physrevlett.123.225101.

[58] A. Zeiler, D. Biskamp, J. Drake, B. Rogers, M. Shay, and M. Scholer, "Three-dimensional particle simulations of collisionless magnetic reconnection," Journal of Geophysical Research **107** (2002), 10.1029/2001ja000287.

[59] C. K. Birdsall and A. B. Langdon, "Plasma physics via computer simulation," (Institute of Physics Publishing, Philadelphia, 1991) Chap. 15.

[60] P. N. Guzdar, J. F. Drake, D. McCarthy, A. B. Hassam, and C. S. Liu, "Three-dimensional fluid simulations of the nonlinear drift-resistive ballooning modes in tokamak edge plasmas," Phys. Fluids B **5**, 3712–3727 (1993).

[61] J. R. Shuster, M. R. Argall, R. B. Torbert, L.-J. Chen, C. J. Farrugia, L. Alm, S. Wang, W. Daughton, D. J. Gershman, B. L. Giles, C. T. Russell, J. L. Burch, and C. J. Pollock, "Hodographic approach for determining spacecraft trajectories through magnetic reconnection diffusion regions," Geophysical Research Letters **44**, 1625–1633 (2017).

[62] L.-J. Chen, W. S. Daughton, B. Lefebvre, and R. B. Torbert, "The inversion layer of electric fields and electron phase-space-hole structure during two-dimensional collisionless magnetic reconnection," Physics of Plasmas **18**, 012904 (2011).

[63] J. Egedal, W. Fox, N. Katz, M. Porkolab, M. Øieroset, R. P. Lin, W. Daughton, and J. F. Drake, "Evidence and theory for trapped electrons in guide field magnetotail reconnection," Journal of Geophysical Research: Space Physics **113**, A12207 (2008).

[64] J. Egedal, A. Lê, Y. Zhu, W. Daughton, M. Øieroset, T. Phan, R. P. Lin, and J. P. Eastwood, "Cause of super-thermal electron heating during magnetotail reconnection," Geophysical Research Letters **37**, L10102 (2010).

[65] J. R. Shuster, D. J. Gershman, J. C. Dorelli, B. L. Giles, S. Wang, N. Bessho, L.-J. Chen, P. A. Cassak, S. J. Schwartz, R. E. Denton, V. M. Uritsky, W. R. Paterson, C. Schiff, A. F. Viñas, J. Ng, L. A. Avanov, D. E. da Silva, and R. B. Torbert, "Structures in the terms of the Vlasov equation observed at Earth's magnetopause," Nature Physics **17**, 1056–1065 (2021).

[66] A. Delgado-Bonal, "Entropy of radiation: the unseen side of light," Scientific Reports **7**, 1642 (2017).

[67] E. Kawamori, "The H-theorem for the entropy of waves," Physics Letters A **400**, 127315 (2021).

[68] T.-W. Lee, "Scaling of the maximum-entropy turbulence energy spectra," European Journal of Mechanics - B/Fluids **87**, 128–134 (2021).

[69] P. Shi, P. Srivastav, C. Beatty, R. S. Nirwan, and E. E. Scime, "Incoherent Thomson scattering system for PHAse space MApping (PHASMA) experiment," Review of Scientific Instruments **92**, 033102 (2021), _eprint: https://doi.org/10.1063/5.0040606.

[70] K. G. Klein, O. Alexandrova, J. Bookbinder, D. Caprioli, A. W. Case, B. D. G. Chandran, L. J. Chen, T. Horbury, L. Jian, J. C. Kasper, O. L. Contel, B. A. Maruca, W. Matthaeus, A. Retino, O. Roberts, A. Schekochihin, R. Skoug, C. Smith, J. Steinberg, H. Spence, B. Vasquez, J. M. TenBarge, D. Verscharen, and P. Whittlesey, "[Plasma 2020 Decadal] Multipoint Measurements of the Solar Wind: A Proposed Advance for Studying Magnetized Turbulence," (2019), _eprint: 1903.05740.

[71] A. Chasapis, W. H. Matthaeus, T. N. Parashar, M. Wan, C. C. Haggerty, C. J. Pollock, B. L. Giles, W. R. Paterson, J. Dorelli, D. J. Gershman, R. B. Torbert, C. T. Russell, P.-A. Lindqvist, Y. Khotyaintsev, T. E. Moore, R. E. Ergun, and J. L. Burch, "In Situ Observation of Intermittent Dissipation at Kinetic Scales in the Earth's Magnetosheath," The Astrophysical Journal **856**, L19 (2018), publisher: American Astronomical Society.

[72] J. L. Burch, "Data from NASA's Magnetospheric Multiscale (MMS) mission," (2015).

[73]M. R. Argall, C. R. Small, S. Piatt, L. Breen, M. Petrik, K. Kokkonen, J. Barnum, K. Larsen, F. D. Wilder, M. Oka, W. R. Paterson, R. B. Torbert, R. E. Ergun, T. Phan, B. L. Giles, and J. L. Burch, "MMS SITL Ground Loop: Automating the Burst Data Selection Process," Frontiers in Astronomy and Space Sciences **7**, 54 (2020).

[74]M. R. Argall, C. R. Small, and M. Petrik, "PyMMS: A Python Library for NASA's Magnetospheric Multiscale (MMS) Mission," (2020).

[75]M. R. Argall, M. H. Barbhuiya, P. A. Cassak, S. Wang, J. Shuster, H. Liang, D. Gershman, R. B. Torbert, and J. L. Burch, "Data for Theory, Observations, and Simulations of Kinetic Entropy in a Magnetotail Electron Diffusion Region," (2021).